Redox Evolution via Gravitational Differentiation on Low-mass Planets: Implications for Abiotic Oxygen, Water Loss, and Habitability

R. D. Wordsworth[1,2], L. K. Schaefer[3], and R. A. Fischer[2]
[1] School of Engineering and Applied Sciences, Harvard, Cambridge, MA 02138, USA
[2] Department of Earth and Planetary Sciences, Harvard, Cambridge, MA 02138, USA; rwordsworth@seas.harvard.edu
[3] School of Earth and Space Exploration, Arizona State University, Tempe, AZ 85287, USA

Abstract

The oxidation of rocky planet surfaces and atmospheres, which arises from the twin forces of stellar nucleosynthesis and gravitational differentiation, is a universal process of key importance to habitability and exoplanet biosignature detection. Here we take a generalized approach to this phenomenon. Using a single parameter to describe the redox state, we model the evolution of terrestrial planets around nearby M stars and the Sun. Our model includes atmospheric photochemistry, diffusion and escape, line-by-line climate calculations, and interior thermodynamics and chemistry. In most cases, we find abiotic atmospheric O_2 buildup around M stars during the pre-main-sequence phase to be much less than calculated previously, because the planet's magma ocean absorbs most oxygen liberated from H_2O photolysis. However, loss of noncondensing atmospheric gases after the mantle solidifies remains a significant potential route to abiotic atmospheric O_2 subsequently. In all cases, we predict that exoplanets that receive lower stellar fluxes, such as LHS1140b and TRAPPIST-1f and g, have the lowest probability of abiotic O_2 buildup and hence may be the most interesting targets for future searches for biogenic O_2. Key remaining uncertainties can be minimized in future by comparing our predictions for the atmospheres of hot, sterile exoplanets such as GJ1132b and TRAPPIST-1b and c with observations.

Key words: astrobiology – planet–star interactions – planets and satellites: atmospheres – planets and satellites: terrestrial planets – ultraviolet: planetary systems

1. Introduction

Following the recent discoveries of nearby exoplanets with masses in the 1–10 M_E range, we are faced with the exciting prospect that in the near future, characterization of the atmospheres of rocky planets outside the solar system will be possible (Udry et al. 2007; Berta-Thompson et al. 2015; Anglada-Escudé et al. 2016; Gillon et al. 2016; Dittmann et al. 2017; Gillon et al. 2017). Some of these planets, such as GJ1132b or TRAPPIST-1b and c, receive a greater stellar flux than Venus and hence are likely to have hot, possibly molten surfaces (Berta-Thompson et al. 2015; Gillon et al. 2016; Schaefer et al. 2016). Others, such as Proxima Centauri b and LHS1140b, are potentially habitable to Earth-like life, depending on their atmospheric composition (Kasting et al. 1993; Wordsworth et al. 2010b; Pierrehumbert 2011a; Kopparapu et al. 2013; Barnes et al. 2016; Turbet et al. 2016).

Development of a general framework for predicting the atmospheric composition of rocky planets is one of the major theoretical challenges of the field in the coming years. For high-mass planets, atmospheres are invariably hydrogen-dominated, and composition at a given pressure is dominated by a balance between thermo- and photochemical effects (e.g., Moses et al. 2011). For low-mass planets, the bulk atmospheric composition is considerably harder to predict, because the external boundary conditions (escape to space, delivery from planetary embryos and comets, and outgassing/subduction) have a fundamental and still poorly constrained influence (e.g., Morbidelli et al. 2000; Hirschmann & Withers 2008; Lammer et al. 2008; Lenardic & Crowley 2012; Wordsworth & Pierrehumbert 2013; Dong et al. 2017).

Given the complexity of the problem, simplifying assumptions are essential for progress. One useful approach is to limit the number of chemical elements in a model to the bare minimum needed to capture essential features. For example, galactic elemental abundances are such that among the nonnoble volatiles, H, C, N, O, and S can be expected to dominate the composition of almost any planetary atmosphere receiving a stellar flux within an order of magnitude of that received by Earth. However, even for atmospheres restricted to just these elements, the phase space of composition remains extremely large, as evidenced by the diversity of atmospheres in our own solar system.

One potentially fruitful approach is to characterize every atmosphere in terms of a single chemical variable. Appropriately defined, the atmospheric redox state is particularly useful because of the dominant controlling role of redox in atmospheric and surface chemistry (e.g., Yung & DeMore 1999). Redox evolution is also extremely important to astrobiology. First, formation of prebiotic molecules, and hence biogenesis, proceeds most readily on planets with weakly or highly reducing atmospheres and surfaces (Miller & Urey 1959; Zahnle 1986; Powner et al. 2009; Tian et al. 2011; Ranjan & Sasselov 2017). Second, the highly oxidized state of Earth's present-day atmosphere and much of its surface is a product of the biosphere, and hence O_2 has potential as a biosignature, or unique sign of life (Selsis et al. 2002; Kaltenegger et al. 2010; Seager et al. 2012; Zahnle et al. 2013). Nonetheless, it has recently been shown that abiotic processes may lead to buildup of O_2-dominated atmospheres on planets that lack life in some cases (Wordsworth & Pierrehumbert 2014; Luger & Barnes 2015; Schaefer et al. 2016). These cases constitute "false positives" for life that require careful study to discriminate them from biologically generated atmospheres (Domagal-Goldman et al. 2014; Schwieterman et al. 2015; Meadows et al. 2016). A robust understanding of the factors that control a planet's surface and atmospheric redox evolution is
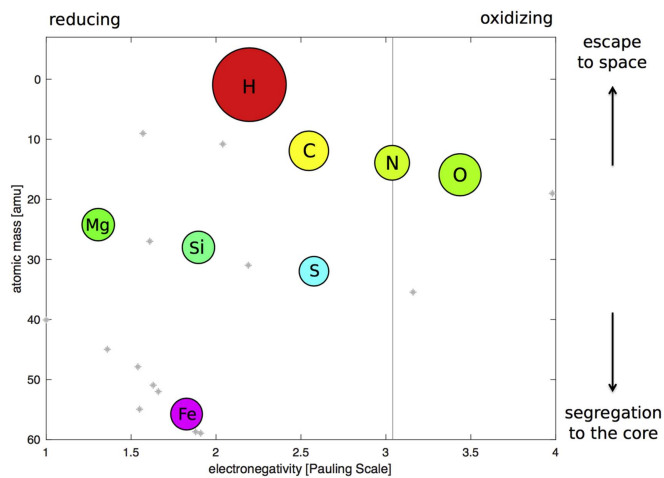
Figure 1. Plot of atomic mass vs. electronegativity for the major elements in the solar system, with the size of the circle corresponding to elemental abundance. Gray asterisks denote elements with abundances lower than 10% of that of Si. Escape to space is dominated by lower-mass elements (particularly H), while higher-mass elements (particularly Fe) tend to segregate to the planet's core. The intermediate-mass, more electronegative elements C, N, and O dominate the atmospheres of the rocky solar system planets. Abundance data are from Lodders (2003), and electronegativity data are from Pauling (1967).

therefore critical for future observational searches for life on other worlds.

Here we take a generalized approach to this problem. We focus on abiotic processes that can cause irreversible oxidation of planetary surfaces and atmospheres, because they are most relevant to biosignature definition and prebiotic chemistry. Extending our previous specific study of the atmospheric evolution of the exoplanet Gliese 1132b (Schaefer et al. 2016), we model both interior–atmosphere exchange and the escape to space of key atomic species. In Section 2, we discuss planetary oxidation from a general perspective. In Section 3, we discuss atmospheric escape, and in Sections 4 and 5, we discuss coupling between the atmosphere and planetary interior. In Sections 6 and 7, we discuss the important issue of H_2O cold-trapping and the role of hydrogen-bearing species other than H_2 and H_2O. The key findings of this work and future directions are discussed in Sections 8 and 9.

2. A Generalized Approach to Planetary Oxidation

While the idea that rocky planets can oxidize abiotically via H_2O photolysis followed by hydrogen loss to space is well-developed (e.g., Oparin 1938; Kasting & Pollack 1983; Chassefière 1996; Wordsworth & Pierrehumbert 2014; Luger & Barnes 2015; Schaefer et al. 2016), the simplicity of the physics driving oxidation is often obscured by the host of other complex effects that can sculpt planetary atmospheres, not to mention the interplay between redox and life on Earth. To understand why surface oxidation should be expected as a general rule, it is useful to compare the reducing power and atomic masses of the major elements that make up low-mass planets. Figure 1 shows a plot of the major solar system elements as a function of their electronegativity according to the Pauling scale (Pauling 1967) and their atomic mass. The size of each circle scales with the logarithm of the element's abundance (Lodders 2003). Only elements with solar system abundances of 4×10^{-6} or more relative to hydrogen are displayed.

If we treat solar system element abundances as a proxy for those in exoplanet systems, primordial planetary atmospheres are likely to be dominated by one reducing (low electro-negativity), highly volatile element (H); one oxidizing (high electronegativity) element of intermediate mass (O); and two intermediate elements that are less abundant (C and N). The heaviest major element, Fe, has significant reducing power. The intermediate-mass elements (Na to Ca) have generally low electronegativity but tend to combine rapidly with the more abundant oxygen on condensation in the protoplanetary disk and subsequently remain in the crust and mantle for all but the hottest planets. For most compounds, there is a strong correlation between mean molecular mass and density at a given pressure, and so iron preferentially accumulates in the core and hydrogen preferentially escapes to space. On terrestrial-type planets, gravitational segregation therefore always acts to drive reducing power away from the surface and atmosphere.

Simple as this principle is, it is interesting to note that it depends entirely on the selective effects of stellar nucleosynthesis. The abundance of carbon and oxygen relative to elements such as lithium, beryllium, and boron is a consequence of the physics of helium burning in late-stage stars (Clayton 1968). In a hypothetical universe where lithium was a dominant product of stellar fusion, hydrogen loss would cause an increase in the total reducing power of a planet's surface. Planetary oxidation is probably crucial to the origin and development of complex life, so the fact that lithium is not a major element is a rather fascinating and fortunate outcome of nuclear physics.

If segregation of iron to a planet's core was perfectly efficient and the escape of hydrogen to space was independent of atmospheric composition, constructing a general theory of planetary redox evolution would be easy. However, the escape of hydrogen is strongly dependent on its abundance and chemical form in the atmosphere, the mantle iron content in rocky planets is significant, and the rate of transport of oxygen into the planetary interior is a strong function of the mantle thermal state. In the following sections, we describe our approach to modeling each of these processes.

2.1. A Single Variable for Redox State

For convenience, we begin by defining a single redox variable. We first place all elements on an electronegativity scale and set the zero point equal to the electronegativity of nitrogen.[4] We then categorize each element according to the maximum number of electrons it will exchange in interaction with an element on the other side of the electronegativity divide.[5] For any planetary reservoir, the total oxidizing power N can then be calculated as

$$N = \sum_i N_i p_i, \qquad (1)$$

where N_i is the number of atoms of a given element and p_i is the element's oxidizing potential. Frequently, we will be

---

[4] This is a somewhat arbitrary choice, but it fits our emphasis on the interaction between the abundant oxidizing element O and the other key constituents. It also fits with the fact that nitrogen is not a major reducing or oxidizing agent compared to H, O, or Fe.

[5] Emphasis on the most abundant elements here allows us to ignore the wider range of oxidation states that may occur in combination with other elements, e.g., Fe^{6+} in K_2FeO_4. These states are important to chemistry in general but not to bulk planetary evolution.

Table 1
Oxidizing Potential (as Defined in the Main Text) and Solar and BSE
Abundances (Atomic Fraction) of the Major Planetary Elements

Element	p_i	Solar Abundance	BSE Abundance
H	−1	24300	$<4.0 \times 10^{-2}$
C	−4	7.08	5.9×10^{-3}
N	0	1.95	1.6×10^{-5}
O	+2	14.13	3.76
Mg	−2	1.02	1.28
Al	−3	0.084	0.10
Si	−4	1.0	1.0
S	−6	0.45	$<1.0 \times 10^{-3}$
Ca	−2	0.063	0.075
Fe	−3	0.84	0.14

Note. Abundances are defined relative to Si and are from Lodders (2003; solar), Marty (2012; BSE H, C, and N), and Javoy (1999; BSE other elements).

working with large numbers of atoms, so it is convenient to express N in terms of the total amount of accessible electrons in the hydrogen in Earth's oceans ($N_{e,\text{TO}} = 9.15 \times 10^{46}$). The oxidizing potential for 10 major elements, alongside their solar and bulk silicate Earth (BSE) abundances, is given in Table 1. This approach bears some similarity to schemes proposed to describe the redox budget of planetary atmospheres in the past (e.g., Kasting & Brown 1998), but its direct link to elemental electronegativity allows for more systematic classification.

After formation, all planets in the 1–10 Earth mass range are predicted to differentiate into an iron-dominated core, a silicate mantle, and a volatile layer containing lighter species. In the simplest terms, the abiotic redox evolution problem can then be framed as the exchange of oxidizing power between these three reservoirs (Figure 2), such that

$$\dot{N}_a = -k_1 N_a + k_2 N_b + E(t), \tag{2}$$

$$\dot{N}_b = +k_1 N_a - (k_2 + k_3) N_b + k_4 N_c, \tag{3}$$

$$\dot{N}_c = +k_3 N_b - k_4 N_c. \tag{4}$$

Here N_a, N_b, and N_c are the total oxidizing power of the volatile layer, silicate mantle, and core; k_{1-4} are exchange terms (see Figure 2); and $E(t)$ captures oxidation due to preferential atmospheric escape of hydrogen. Situations where the value of N_a becomes positive are of particular importance to us, because this is when O_2 and other oxidizing species will begin to accumulate in the volatile layer.

The size of the exchange terms k_{1-4} is strongly dependent on the phases of the layers in question. For example, on present-day Earth with a solid silicate mantle, the value of k_1 and k_2 is of order Gy^{-1}. In contrast, on a newly formed planet with a liquid silicate layer (magma ocean), k_1 and k_2 have characteristic values of weeks^{-1} to days^{-1} (Solomatov 2007). However, because magma oceans may only extend across a given region in the mantle (Abe 1997; Lebrun et al. 2013; Schaefer et al. 2016), treatment of separate solid and liquid silicate reservoirs is important.

If magma oceans solidify from deep in the mantle upward, the exchange rates between the core and mantle (k_{3-4}) will be low as soon as the main period of planetary differentiation is complete, and Equation (4) can be neglected. Here we make the simplification that the core formation period occurs quickly and hence sets the initial condition for the mantle's oxidizing power
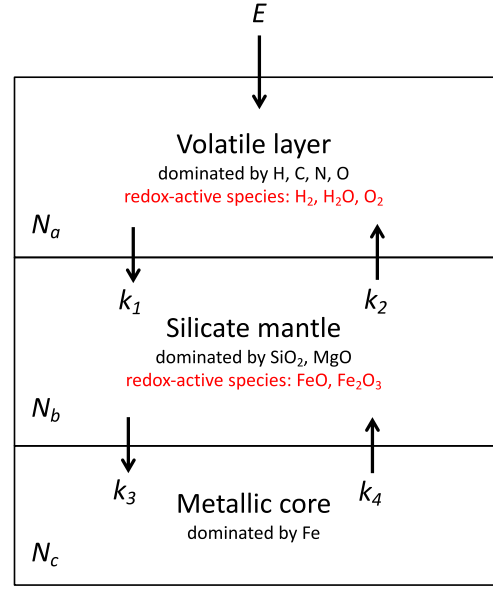

Figure 2. Schematic of the box-model approach to planetary redox flow, with layers defined in terms of bulk composition. Differential escape preferentially removes hydrogen and hence represents a positive flux of net oxidizing power.

N_b in our model. After this point, we assume zero exchange between regions b and c. This assumption is most justified for planets around M stars, which are expected to have long-lived magma oceans due to their host stars' extended pre-main-sequence phases. The physics and chemistry of core formation in general are discussed next.

2.2. The Lower Boundary Condition: Core Formation and Initial Mantle Composition

During core formation, chemical interactions between the molten mantle and core materials at high pressures (p) and temperatures (T) set the redox state of the mantle, and thus N_b. As a planet grows larger, the average pressure and temperature of metal–silicate equilibration, which likely occurs in or at the base of the magma ocean in the silicate layer (Stevenson 1981; Rubie et al. 2003), are both generally considered to increase (Rubie et al. 2011; Fischer et al. 2017).

At very high pressures and temperatures, some elements that are less electronegative than Fe on the Pauling scale will accept electrons (give up oxygen atoms), becoming neutral and dissolving into the core as metals. This complicates the simple picture of clean separation between elements suggested by Figure 1. The most important of these less-electronegative elements in terms of planetary redox changes is silicon (Siebert et al. 2012; Tsuno et al. 2013; Fischer et al. 2015), which undergoes the reaction $Si^{4+} + 4e^- \rightarrow Si^0$. This half of the redox reaction is balanced by more electronegative (Pauling scale) elements donating electrons to oxygen atoms, forming silicates and oxides and entering the mantle. Most importantly, Fe oxidizes from its metallic form to enter the mantle as ferrous iron, leading to the overall reaction

$$Si^{4+} + 2Fe^0 \rightarrow Si^0 + 2Fe^{2+}. \tag{5}$$
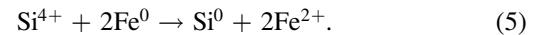
This transfer of electrons from Fe to Si is the primary mechanism for increasing a planet's mantle FeO inventory during core formation (Ringwood 1959; Rubie et al. 2011, 2015; Fischer et al. 2017). It can change the composition of the mantle

significantly, increasing the FeO content by a factor of around three (Fischer et al. 2017) or more (Rubie et al. 2011, 2015). However, reactions occurring during core formation do not significantly alter the composition of the core itself, except for the addition of some light elements like Si and O; its iron content does not change significantly for planets near an Earth mass (e.g., Rubie et al. 2011, 2015; Fischer et al. 2017).

In planets that are larger than an Earth mass, the pressures and temperatures of metal–silicate equilibration will be higher. At higher pressures and particularly at higher temperatures, reaction (5) will proceed farther to the right (Siebert et al. 2012; Fischer et al. 2015), leading to larger redox changes and a higher mantle FeO content and hence a more negative initial value of N_b. Plausibly, planets that are hotter during formation for other reasons (such as more energetic impacts during accretion) will also have higher mantle FeO content.

In core formation studies, it is standard to refer to the addition of FeO to the mantle as a net oxidation of the mantle, because Fe loses electrons to O when it is removed from the core. However, from an atmospheric/surface perspective, the most important outcome of reaction (5) is that the iron added to the mantle can be further oxidized to Fe^{3+} and hence constitutes a potential sink of oxidizing power (more negative value of N_b in our scheme). This discrepancy of terminology is probably linked to the fact that FeO is the most oxidized iron species under core–mantle boundary conditions, while Fe_2O_3 is the most oxidized form of iron on planetary surfaces.

Existing models of core–mantle equilibration during accretion for the inner solar system planets yield FeO mantle abundances ranging from 6 to 20 wt%, in approximate agreement with estimates of Earth, Venus, Mars, and Mercury's actual mantle iron content (Fischer et al. 2017). Here we vary the initial mantle FeO content from 0 to 20 wt%. Nonetheless, we regard 5 wt% as a plausible lower limit in all but the most extreme cases.

Though Si plays an important role in planetary redox during core formation, mantle silicon is subsequently bonded with oxygen and mainly remains in the silicate mantle without any valence changes. Likewise, Mg, Al, and Ca readily bond with the more abundant O in protoplanetary disks and subsequently mainly remain in the silicate mantle. Here these elements, as well as Si, are neglected in the overall redox budget, but Fe is included. Because it is relatively scarce in the BSE, we also neglect S here, although it may play an important role in certain cases. Finally, C and N species (particularly CO_2, CH_4, and N_2) can have important atmospheric effects, but their direct contribution of these elements to the redox budget is also typically smaller than that of O and H. The contributions of CO_2 and N_2 to the greenhouse effect and atmospheric cold-trapping of H_2O are considered in Sections 4 and 5. However, in the redox evolution modeling, the only active species we allow are H, O, and Fe.

2.3. Redox Disproportionation of Fe

Besides direct interaction of the silicate melt with the core, a second potentially important influence on planetary redox evolution during the late stages of core formation is Fe redox disproportionation. This becomes important when the crystallization pressures are greater than about 24 GPa[6] and the

mineral bridgmanite [$MgSiO_3$] is stable (e.g., Fei et al. 2004). At these pressures, Fe^{3+} can incorporate into bridgmanite in the reaction (Frost et al. 2004)

$$3Fe^{2+} \rightarrow Fe^0 + 2Fe^{3+}. \qquad (6)$$
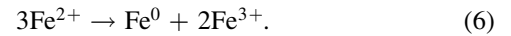
This reaction is more likely when abundances of Al are high, due to a coupled substitution of $Fe^{3+} + Al$ for $(Mg, Fe^{2+}) + Si$ in bridgmanite (e.g., Frost et al. 2004). The metallic iron produced in this reaction is higher density and hence migrates to the core, leaving behind oxidized Fe^{3+} in the mantle. This reaction thus serves to oxidize the mantle, making N_b less negative. As with reaction (5), reaction (6) will be more efficient in larger planets, due to the greater depth range over which bridgmanite and post-perovskite ($MgSiO_3$, which can similarly incorporate Fe^{3+} into its structure; Catalli et al. 2010) are stable.

It is interesting to note that in a very general sense, Fe disproportionation can be viewed as simply another example of the process of redox gradient formation via gravitational differentiation. The equilibrium constant of reaction (6) depends on pressure (and hence gravity) via the net volume change of the reaction (O'Neill et al. 2006). In situations where disproportionation is favored, the atoms rearrange themselves to minimize Gibbs energy, causing denser metallic iron to sink to the core and the less dense Fe^{3+} compounds to remain in the mantle.

Our understanding of the importance of reaction (6) is still limited by the availability of experimental data. As we show in Section 5, the upper mantle Fe^{3+}/Fe^{2+} ratio needs to reach around 0.3 or more before volcanic outgassing (the k_2N_b term in Equation (2)) becomes a source of net oxidizing power. If in situations where Al is abundant or p and T are high, reaction (6) becomes extremely effective (e.g., on high-mass planets), Fe redox disproportionation could contribute significantly to the eventual buildup of abiotic O_2 in the atmosphere. Further experimental study to constrain this issue better in future will be useful.

2.4. Initial Abundances of H_2 and H_2O

Besides the stellar properties, planet mass and radius, and mantle FeO abundance, the other key initial conditions required for redox evolution modeling are the volatile-layer abundance of H_2 and H_2O. Hydrogen may be delivered to low-mass planets by direct nebular capture (Rafikov 2006) or possibly oxidation of metallic iron by H_2O (Kuramoto & Matsui 1996). The presence of an initial H_2 envelope is equivalent to starting with an extremely negative value of N_a in Equations (2) and (3): it inhibits atmospheric oxidation until all of the H_2 is lost to space. Our main aim here is to obtain upper limits on atmospheric O_2 buildup, so in our models, we make the assumption that the starting H_2 inventory is negligible. For H_2O, we treat the initial abundance as a free parameter varying between 0 and 1 wt%.[7] The densities of planets with H_2O abundances above a few percent are likely to be sufficiently elevated to allow them to be distinguished from less volatile rich cases (Zeng & Sasselov 2013).

---

[6] For comparison, Earth's core–mantle boundary pressure is approximately 140 GPa.

[7] For reference, on Earth, the total mass of the surface ocean (1 TO) is 230 ppmw or 0.023 wt%, while the total mantle H_2O abundance is somewhere between 0.2 and 13 TO (Hirschmann & Dasgupta 2009; Marty 2012).

3. The Upper Boundary Condition: Atmospheric Escape of H

The final boundary condition we need to incorporate to solve Equations (2)–(4) is the escape term E. Atmospheric escape is a complex process that is still incompletely understood. However, of the diverse range of possible atmospheric escape processes, Jeans escape is almost always negligible, while for the escape of heavy elements such as C and O, ion-driven processes and sputtering are most important (e.g., Lammer et al. 2008). In general, processes driven by the stellar wind appear capable of removing up to tens of bars of gas from planetary atmospheres around G- and M-class stars (Airapetian et al. 2017; Dong et al. 2017; Zahnle & Catling 2017). These quantities are potentially significant for heavy gases (particularly N_2; Section 6) but not for H_2 or H_2O: the equivalent partial pressure of one terrestrial ocean (TO) on Earth is 263 bar. Impact-driven escape can be significant (Ahrens 1993; Zahnle & Catling 2017) but does not fractionate gas species. In contrast, extreme ultraviolet (XUV)–driven hydrodynamic escape is capable of removing large quantities of volatiles and always preferentially removes hydrogen as long as it is abundant in the planet's upper atmosphere. For these reasons, it is probably the key process driving redox evolution via escape for planetary atmospheres early in their evolution, and it is what we focus on here.

In the absence of any other limits, the ultimate constraint on the rate of XUV-driven escape is the total supply of XUV energy. This leads to the well-known escape rate formula (e.g., Watson et al. 1981; Zahnle 1986)

$$\phi_E = \frac{\epsilon F_{XUV}}{4 V_{pot}}, \tag{7}$$

where ϕ_E is a mass flux ($kg^{-1}\,m^{-2}\,s^{-1}$), F_{XUV} is the stellar flux in the XUV wavelength range suitable for ionizing hydrogen ($\sim$10–91 nm), and $V_{pot} = GM_p/r_p$ is the gravitational potential at the base of the escaping region, with G the gravitational constant and M_p and r_p the planetary radius and mass, respectively. Here ϵ is an efficiency factor, which we discuss further in Section 3.2.

The upper portions of planetary atmospheres may be hydrogen-rich due to the presence of H_2 from volcanic outgassing or a primordial envelope, in which case the oxidation rate is simply $E = 4\pi r_p \phi_E/m_p$, where m_p is the proton mass. However, if H_2 is not present, further oxidation can only occur via the photolysis of hydrogen-bearing molecules, of which H_2O is the most important. Then, the extent to which H_2O is cold-trapped in the deep atmosphere, the rate at which it is photolyzed in the upper atmosphere, and the rate at which hydrogen diffuses through the homopause all become important (Figure 3). Cold-trapping is important in a planet's later stages of evolution, once the surface has solidified, and we reserve discussion of it until Section 5. Diffusion and photochemistry are modeled in the next section, while the escape efficiency is constrained in Section 3.2.

3.1. Diffusion and Atmospheric Photochemistry

During XUV-driven hydrodynamic escape, the composition of the escaping gas, and hence the rate of oxidation of the planet, depends critically on the rate at which products from UV photolysis occurring deeper in the atmosphere diffuse upward. When diffusion is efficient, the dominant escaping
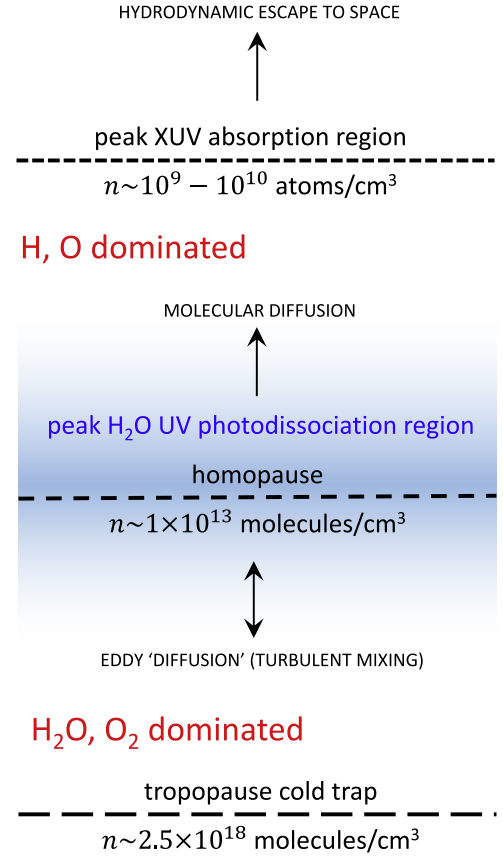

Figure 3. Schematic showing the key regions in a planetary atmosphere undergoing oxidation via H_2O photolysis and hydrogen loss to space. The approximate number density of each region is also indicated.

species will be H, with heavier atoms dragged along to an extent that depends on the total flux. In the limit when diffusion is extremely slow or when photolysis products are efficiently recycled, preferential escape of H could be choked off, and net oxidation of the planet would not occur. In this section, we model upper-atmosphere diffusion and photochemistry to elucidate this critical part of the planetary oxidation problem. Readers not interested in the details should skip to Section 3.3, where we summarize the main results.

Water is photolyzed by UV radiation of wavelength <195 nm via a number of reactions, the most important of which is

$$H_2O + h\nu \rightarrow OH + H. \tag{8}$$
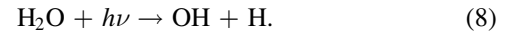
Once atomic H is liberated, it may either react with other atmospheric species or escape to space. When the escape flux is low, H will escape alone, but once it exceeds a critical value, heavier species will also be dragged along. Given a total mass flux ϕ, the number flux (atoms $m^{-2}\,s^{-1}$) of a light species Φ_1 and a heavy species Φ_2 per unit surface area can be calculated as a function of their molar concentrations x_i and atomic/molecular masses m_i as

$$\Phi_1 \approx \begin{cases} \phi/m_1 & : \phi < \phi_c \\ [x_1\phi + x_1 x_2 (m_2 - m_1)\Phi_{d,2}]/\overline{m} & : \phi \geqslant \phi_c \end{cases} \tag{9}$$

and

$$\Phi_2 \approx \begin{cases} 0 & : \phi < \phi_c \\ [x_2\phi + x_1 x_2 (m_1 - m_2)\Phi_{d,1}]/\overline{m} & : \phi \geqslant \phi_c. \end{cases} \quad (10)$$

Here $\overline{m} = m_1 x_1 + m_2 x_2$ is the mean molecular/atomic mass of the flow. The $\Phi_{d,i}$ are equivalent diffusion fluxes, defined as

$$\Phi_{d,i} \equiv \frac{b}{H_i}, \quad (11)$$

where b is the binary diffusion coefficient for the two species and H_i is the effective scale height of species i at the base of the escaping region. The quantity ϕ_c is the critical mass flux required to initiate drag of the heavy species 2 along with the light species 1. It is defined as

$$\phi_c = \Phi_{d,1} x_1 (m_2 - m_1) = \frac{b x_1}{H_1}(m_2 - m_1). \quad (12)$$

This result is easily derived from Equation (10) by noting that the two definitions of Φ_2 must equal each other when $\phi = \phi_c$ and using the scale height definition $H_i = k_B T / m_i g$, where g is gravity, k_B is Boltzmann's constant, and T is temperature. The familiar expression for diffusion-limited escape of a light minor species through a heavier, nonescaping species simply corresponds to $\Phi_1 = \phi_c / m_1$, or

$$\Phi_1 = b x_1 (H_2^{-1} - H_1^{-1}). \quad (13)$$

If species 1 is H and species 2 is H_2O or O_2, we can write

$$\Phi_{\mathrm{H,diff}} \approx \frac{b x_{\mathrm{H}}}{H_s}, \quad (14)$$

where H_s is the scale height of the background gas. Equations (9)–(12) are completely equivalent to the "cross-over-mass" formalism of Hunten et al. (1987) but are considerably more straightforward to work with. Their derivation from first principles is given in Appendix A.

The extreme upper limit on the rate of H liberation during photolysis comes from the supply of UV photons to H_2O. However, depending on the atmospheric composition, other chemical pathways may remove H rapidly once it is created. This may be particularly important in an atmosphere that has already begun to build up some O_2. Classic studies of martian photochemistry (McElroy & Donahue 1972; Yung & DeMore 1999) have shown that the three-body reaction,

$$\mathrm{H} + \mathrm{O}_2 + \mathrm{M} \rightarrow \mathrm{HO}_2 + \mathrm{M}, \quad (15)$$
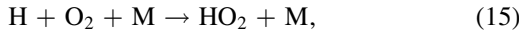
where M is a background gas molecule, is a key step in the recycling of H when O_2 is present. Once HO_2 has formed, combination with the OH radical

$$\mathrm{OH} + \mathrm{HO}_2 \rightarrow \mathrm{H}_2\mathrm{O} + \mathrm{O}_2 \quad (16)$$
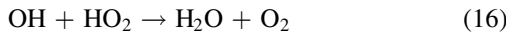
closes the cycle, leading to stabilization of H_2O against photolysis. On present-day Mars, which has an H_2O-poor upper atmosphere, this means that hydrogen escape depends on a minor pathway to form H_2, and H escape is regulated until O and H escape in a 1:2 ratio. However, Mars' crust appears to have oxidized extensively relative to its mantle (Wadhwa 2001), which provides a hint that reaction (15) may not effectively limit H escape under all circumstances.

Table 2
Values of the Binary Diffusion Coefficient b Used in the Photochemical and Escape Calculations for Various Interacting Species

Species	b (molecules cm^{-1} s^{-1})
O, O(^{1}D) in H_2O	$1.06 \times 10^{17}T^{0.774}$
H in H_2O	$6.6 \times 10^{17}T^{0.7}$
H in O	$4.8 \times 10^{17}T^{0.75}$
H_2 in H_2O	$2.7 \times 10^{17}T^{0.75}$
All others	$1.37 \times 10^{16}T^{1.072}$

Note. Data for all species were taken from Zahnle (1986) and cross-checked versus data in Marrero & Mason (1972).

To understand the relative importance of chemical and diffusive effects, we have performed simulations using a one-dimensional photochemical model (Wordsworth 2016a). Our model calculates the number density time evolution for a given species n_i via the equation

$$\frac{\partial n_i}{\partial t} + \frac{\partial \Phi_i}{\partial z} = P_i - L_i. \quad (17)$$

Here n_i is the number density of species i, and P_i and L_i are the rate of chemical production and loss, and $\Phi_i(z)$ is the number flux due to transport processes. It is defined here as

$$\Phi_i = -Kn \frac{\partial}{\partial z}\left(\frac{n_i}{n}\right) - Dn_{i,e} \frac{\partial}{\partial z}\left(\frac{n_i}{n_{i,e}}\right), \quad (18)$$

where $n_{i,e} \propto e^{-z/H_i}$, $n \propto e^{-z/H}$, H is the mean scale height of the atmosphere, K is the eddy diffusion coefficient, and $D = b/n$, with b the binary molecular diffusion coefficient and n the total number density (Yung & DeMore 1999). We treat K as constant with height, with a nominal value of 10^5 cm^2 s^{-1}. Our representation of b is summarized[8] in Table 2.

Photodissociation reaction rates are calculated as

$$J_k(z) = \frac{1}{4}\int_{\lambda_1}^{\lambda_2} Q_k(\lambda)\sigma_k(\lambda)F_{\mathrm{UV}}(z, \lambda)d\lambda, \quad (19)$$

where λ is wavelength; σ_k and Q_k are the absorption cross-section and quantum yield of photoreaction k, respectively; and F_{UV} is the incoming stellar UV flux at wavelengths below $\lambda_2 = 195$ nm. The nominal spectrum for F_{UV} is shown in Figure 4; see Section 3.3 for a discussion of our treatment of M-star UV spectra and temporal evolution. The factor of 1/4 accounts for day–night averaging and the mean angle of propagation (assumed to be 60° here). In the nominal simulations, we allow both UV and XUV radiation to contribute to photolysis,[9] setting $\lambda_1 = 1$ nm. Here $F_{\mathrm{UV}}(z, \lambda)$ is calculated in each layer from the number density and total absorption cross-section assuming a mean propagation angle of 60°. The average value of $J_k(z)$ is then used when solving Equation (17).

---

[8] The "all others" category in Table 2 uses data for O_2 in H_2O. Although data are not available for every possible interacting pair, differences between b values among species are small in general. Because we are most interested in order-of-magnitude changes to escape rates, our use of a reduced set of b values here is unlikely to have a significant impact on our results.
[9] We tested the effects of removing all of the XUV radiation used to power escape first and found that the influence on our results was insignificant.
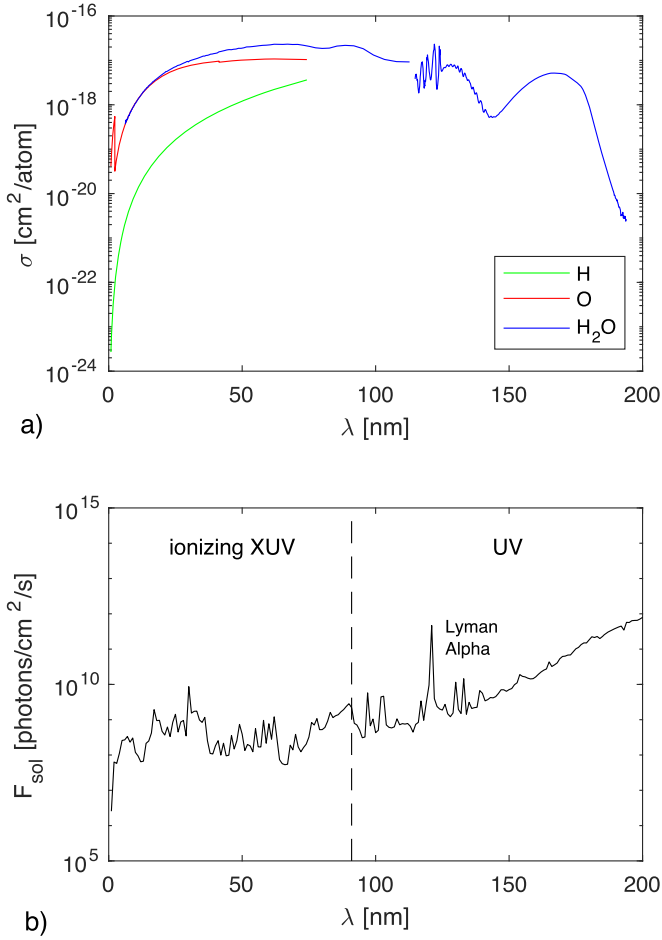
Figure 4. (a) Photoionization cross-sections for H and O and photodissociation cross-section for H_2O as a function of wavelength, based on data from Yeh & Lindau (1985), Yeh (1993), Chan et al. (1993b), and Mota et al. (2005). (b) Present-day solar flux at Earth orbit across the same wavelength range, based on data from Thuillier et al. (2004).

We solve this coupled system of equations for 10 chemical species and 50 vertical layers using an adaptive timestep semi-implicit Euler method with the reaction rate coefficients given in Table 3. The calculation is continued until a steady state is reached, which we check by observing the time evolution of all species at the top and bottom boundaries of the model. Our diffusion scheme, which is based on a weighted centered finite difference, has been tested versus analytic results and verified to conserve molecules to high precision.

In previous studies focused on abiotic oxygen production in Earth-like atmospheres, strong emphasis was placed on the ability of photochemical models to satisfy redox balance (e.g., Domagal-Goldman et al. 2014; Harman et al. 2015), usually defined simply as "conservation of free electrons" (Harman et al. 2015). This emphasis is important for problems where the total oxidation state of the atmosphere + oceans N_a is assumed to remain constant with time. Because our photochemical model conserves atoms to high precision, it also conserves free electrons. This does not mean that the number of free electrons in the atmosphere necessarily remains constant before equilibrium is reached in our simulations, as we allow for the possibility of O and H fluxes through the top and bottom model boundaries, which evolves the atmospheric composition. However, our coupled approach to redox flow (Figure 2) means that in later sections, when we link the atmosphere with

the planetary interior, the global number of accessible electrons $N_e = -(N_a + N_b + N_c)$ is only altered by the escape to space term $E(t)$. Hence, our model satisfies redox balance according to the standard definition. Importantly, it has the additional advantage of requiring no ad hoc assumptions about the redox state of the mantle after the initial conditions have been set.

The photochemical model domain is defined from 10^4 Pa at the base to 10^{-5} Pa at the top, to encompass the entire range over which H_2O photolysis is important. We have confirmed that our results are insensitive to increases in this pressure range. We initialize the atmosphere with constant molar concentrations of H_2O and O_2, and the abundances of all other species are set to zero. The default boundary condition is zero flux (Neumann) at the top and bottom of the model. For H_2O and O_2, we use Dirichlet boundary conditions at the bottom of the model to keep their molar concentrations fixed. For H, we force the molar concentration gradient to be zero at the top boundary, corresponding to diffusion-limited escape.

Figure 5 shows the results of an example calculation with Earth-like UV and XUV insolation, $K = 10^5\,\mathrm{cm^2\,s^{-1}}$, and O_2 molar concentration of $0.5\,\mathrm{mol\,mol^{-1}}$ at the base of the domain. The atmospheric composition is dominated by H_2O, O_2, OH, and H, with O and O_3 existing as minor constituents near the top and base of the domain, respectively. Here the H escape rate is $\Phi_{\mathrm{H,diff}} = 8.3 \times 10^{11}$ atoms $\mathrm{cm^{-2}\,s^{-1}}$. For comparison, the extreme upper limit on the H_2O photolysis rate is the total accessible UV photon flux

$$\Phi_{\mathrm{H,UV}} = \frac{1}{4} \int_{\lambda_1}^{\lambda_2} F_{\mathrm{UV}}(z, \lambda) d\lambda. \qquad (20)$$

For present-day Earth, $\Phi_{\mathrm{H,UV}} \approx 1.9 \times 10^{12}$ atoms $\mathrm{cm^{-2}\,s^{-1}}$, or about 15 times larger than the energy-limited escape rate for hydrogen atoms, $\Phi_{\mathrm{H,E}} = m_p \phi_E$. Obviously, both $\Phi_{\mathrm{H,UV}}$ and $\Phi_{\mathrm{H,E}}$ vary with the incident stellar flux.

As can be seen, there is a sharp decline in the concentration of H below a given depth, due to the rapid increase in the rate of reaction (15) with depth. Because reaction (15) occurs at a rate $\partial n_{\mathrm{H}}/\partial t = -k_3 n n_{\mathrm{O}_2} n_{\mathrm{H}}$, with k_3 defined by C3 in Table 3, the total number density n_b at which this transition occurs in equilibrium can be estimated as

$$n_b^2 \sim \frac{1}{k_3 x_{\mathrm{O}_2} \tau_{\mathrm{diff}}}, \qquad (21)$$

with x_{O_2} defined at n_b and $\tau_{\mathrm{diff}} = H_s^2/(K + D)$ a characteristic timescale for diffusion of H. Equation (21) is easily solved in general, but for situations where the transition occurs above the homopause, as in Figure 5, it can be simplified further to

$$n_b \sim \sqrt[3]{\frac{b}{k_3 x_{\mathrm{O}_2} H_s^2}} . \qquad (22)$$

If we treat the atmosphere above n_b as a single region, the overall H budget can be approximated as a balance between H production and loss. Production comes from H_2O photolysis, while loss must occur through downward eddy diffusion, because molecular diffusion preferentially transports hydrogen upward. Hence,

$$\int_{z_b}^{\infty} P_{\mathrm{H}} dz \approx \Phi_{\mathrm{H,diff}} + \frac{n_{\mathrm{H}} H_s}{\tau_{\mathrm{diff},K}}. \qquad (23)$$

Table 3
Reactions Used in the Photochemical Calculations: (A) Photolysis Reactions, (B) Two-body (Units of cm^3 molecule^{-1} s^{-1}), and (C) Three-body (Units of cm^6 molecule^{-2} s^{-1})

#	Reaction		Rate Coefficient	Reference
A1	H_2	$\xrightarrow{h\nu}$ 2H	From cross-section data	1
A2	O_2	$\xrightarrow{h\nu}$ 2O	From cross-section and quantum yield data	2
A3		$\xrightarrow{h\nu}$ O + O(^{1}D)	From cross-section and quantum yield data	3
A4	H_2O	$\xrightarrow{h\nu}$ OH + H	From cross-section and quantum yield data	4
A5		$\xrightarrow{h\nu}$ H_2 + O(^{1}D)	From cross-section and quantum yield data	4
A6		$\xrightarrow{h\nu}$ 2H + O	From cross-section and quantum yield data	4
A7	OH	$\xrightarrow{h\nu}$ O + H	From cross-section and quantum yield data	4
B1	H + O_3	→OH + O_2	$1.4 \times 10^{-10}e^{-470/T}$	5
B2	H + HO_2	→2OH	7.3×10^{-11}	5
B3		→O + H_2O	2.4×10^{-12}	5
B4		→H_2 + O_2	5.6×10^{-12}	5
B5	O(^{1}D) + O_2	→O + O_2	$3.2 \times 10^{-11}e^{70/T}$	5
B6	O(^{1}D) + O_3	→$2O_2$	1.2×10^{-10}	5
B7		→O_2 + 2O	1.2×10^{-10}	5
B8	O(^{1}D) + H_2	→H + OH	1.2×10^{-10}	5
B9	O(^{1}D) + H_2O	→2OH	$1.63 \times 10^{-10}e^{60/T}$	5
B10	O + OH	→O_2 + H	$1.8 \times 10^{-11}e^{180/T}$	5
B11	O + HO_2	→OH + O_2	$3.0 \times 10^{-11}e^{200/T}$	5
B12	O + H_2O_2	→OH + HO_2	$1.4 \times 10^{-12}e^{-2000/T}$	5
B13	O + O_3	→$2O_2$	$8 \times 10^{-12}e^{-2060/T}$	5
B14	2OH	→H_2O + O	1.8×10^{-12}	5
B15	OH + O_3	→HO_2 + O_2	$1.7 \times 10^{-12}e^{-940/T}$	5
B16	OH + H_2	→H_2O + H	$7.7 \times 10^{-12}e^{-2100/T}$	5
B17	OH + HO_2	→H_2O + O_2	$4.8 \times 10^{-11}e^{250/T}$	5
B18	OH + H_2O_2	→HO_2 + H_2O	1.7×10^{-12}	5
B19	HO_2 + O_3	→OH + $2O_2$	$1.0 \times 10^{-14}e^{-500/T}$	5
B20	HO_2 + HO_2	→H_2O_2 + O_2	$2.3 \times 10^{-13}e^{600/T}$	5
C1	O + O	$\xrightarrow{M}$ O_2	$k = 1.1 \times 10^{-27}T^{-2}$	6
C2	H + H	$\xrightarrow{M}$ H_2	$k = 1.8 \times 10^{-30}T^{-1}$	5
C2	H + H	$\xrightarrow{M}$ H_2	$k = 1.1 \times 10^{-29}T^{-1}$	6
C3	H + O_2	$\xrightarrow{M}$ HO_2	$k_0 = 1.3 \times 10^{-27}T^{-1.6}$, $k_\infty = 7.5 \times 10^{-11}$	6
C4	OH + OH	$\xrightarrow{M}$ H_2O_2	$k_0 = 1.7 \times 10^{-28}T^{-0.8}$, $k_\infty = 1.5 \times 10^{-11}$	6
C5	HO_2 + HO_2	$\xrightarrow{M}$ H_2O_2 + O_2	$k = 1.2 \times 10^{-31}$	6
C6	O + O_2	$\xrightarrow{M}$ O_3	$k = 2.989 \times 10^{-28}T^{-2.3}$	5

Note. Photodissociation cross-sections and quantum yields are taken from the same sources as in Venot et al. (2012), with the exception of O_2.
References. (1) Samson & Haddad (1994), Chan et al. (1992), Olney et al. (1997); (2) Sander et al. (2009); (3) Brion et al. (1979), Yoshino et al. (1992), Chan et al. (1993a), Fally et al. (2000); (4) Chan et al. (1993b), Mota et al. (2005), Huebner et al. (1992); (5) Linstrom & Mallard (2001); (6) Yung & DeMore (1999).

Here z_b is the altitude at which $n = n_b$, $P_H \approx J_{H_2O}n_{H_2O}$, and $\tau_{\text{diff},K} = H_s^2/K$ is the timescale for eddy diffusion of H downward into the lower atmosphere. Assuming $x_{O_2} \approx 1 - x_{H_2O}$ and making use of the diffusion-limited escape Equation (14), we can rearrange to get

$$\Phi_{H,\text{diff}} \approx \frac{\int_{z_b}^{\infty} J_{H_2O}n_{H_2O}dz}{1 + Kn_b/b}. \quad (24)$$

Figure 6 compares this result with the H loss rate calculated by the model as a function of the base O_2 molar concentration. As can be seen, in both cases, the escape rate of hydrogen steadily decreases as O_2 builds up in the atmosphere. The analytic prediction does a reasonable job despite its simplicity, indicating that we have captured the key features of the one-dimensional model. The small systematic underprediction of the model results is due to the neglect of additional O–H reactions that recycle H after interaction with O_2, as is clear from the intercomparison with all additional reactions removed (green lines). While there are variations, to a first approximation, the decrease in Φ_H is linear with x_{O_2}.

Importantly, O_2 molar concentrations below a few percent do not significantly decrease H escape below the O_2-free value. The key reason for this is that the three-body reaction (15) only dominates H removal relatively deep in the atmosphere. Like hydrogen balloons released from an airplane, hydrogen atoms liberated from H_2O above both the homopause and the n_b level mainly escape upward to space, rather than mixing downward. On present-day Mars, the upper atmosphere is extremely poor in H_2O, and most photolysis occurs deeper in the atmosphere. Recent analyses of the Martian atmosphere suggest that loss of atomic H is enhanced when water is able to propagate to the high atmosphere (Chaffin et al. 2017). Our results are consistent with this prediction.
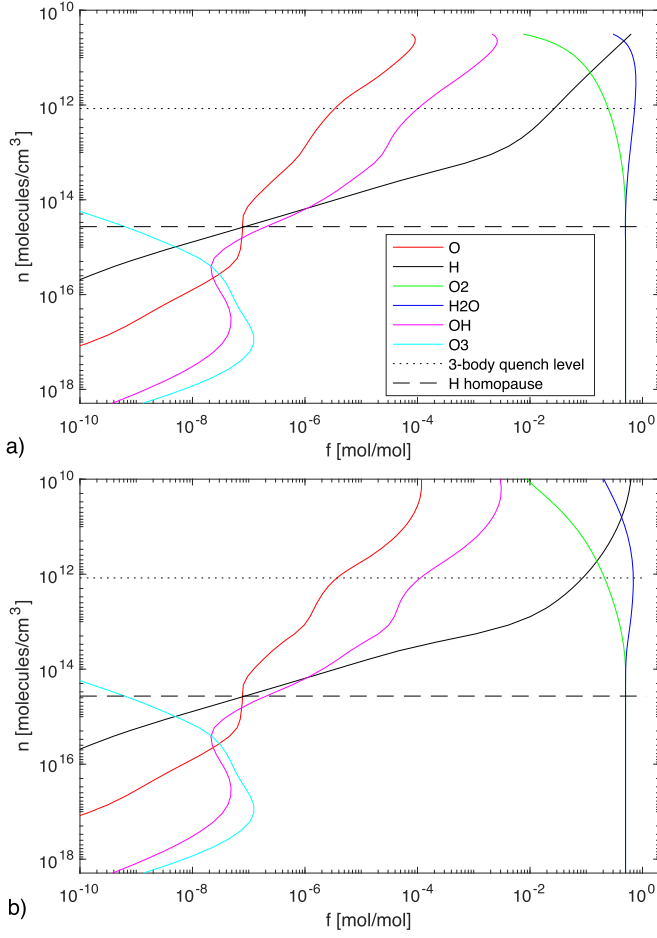
Figure 5. Example output from the one-dimensional photochemical model with (a) fixed and (b) varying total number density and mean scale height. The dashed and dotted lines show the locations of the homopause (for H) and the three-body quench level defined by Equation (21), respectively. In both cases, the H escape rate is 1×10^{12} atoms cm^{-2} s^{-1}.
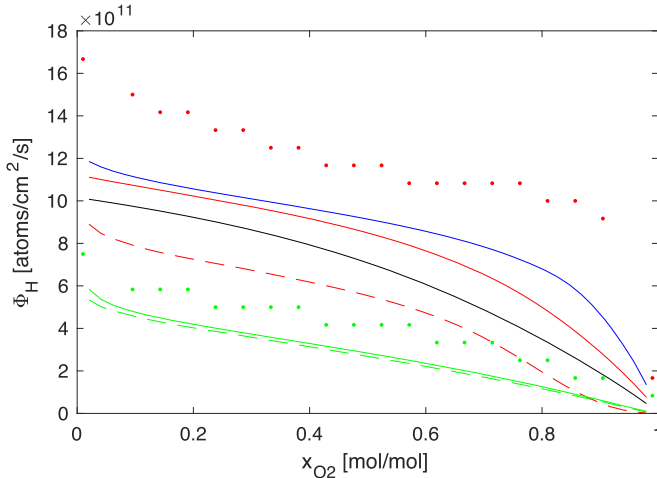

Figure 6. Diffusion-limited H escape rate Φ_H as a function of the O_2 molar concentration of the bulk atmosphere x_{O_2}. Black, red, and blue solid lines show results for $K = 10^4$, 10^5, and 10^6 cm^2 s^{-1}, respectively, while the green solid line shows the results for $K = 10^5$ with all reactions removed except A4 and C3 (see Table 3). The dashed lines show the semi-analytic result (Equation (24)) for the two $K = 10^5$ cm^2 s^{-1} cases. In both cases, the production term $\int_{z_b}^{\infty} J_{H_2O} n_{H_2O} dz$ is derived from the model results. Finally, the dots show H escape upper limits estimated from a code version with varying n and H_s (see main text).

In most simulations, we did not force the total number density n to evolve with time. We regarded this as an acceptable approximation because the escape rate of H is set at either the homopause or n_b, where it is a minor constituent that does not significantly modify n. Nonetheless, as a check on our results, we performed some simulations where n and the mean scale height H_s were allowed to evolve with time in the governing equations. To maintain model stability in these simulations, it was necessary to use a separate Crank–Nicholson scheme for the diffusion solver and a small timestep, resulting in longer simulation times. Figure 5 compares simulations with fixed and varying background profiles for the same boundary conditions. As can be seen, the only significant variation to molar concentrations occurs at the very lowest number densities, well above the n_b level. We also performed n- and H_s-varying simulations where we increased Φ_H until f_H became negative at the top of the atmosphere and recorded the last stable value for Φ_H. The resulting upper limits on Φ_H are displayed as dots in Figure 6. As can be seen, they are within a factor of 1.5 or less of the standard diffusion limits for Φ_H for most values of x_{O_2}. Selected tests at high UV fluxes (not shown) showed similar behavior. Based on this, we decided to keep the standard model setup for our main calculations. The sensitivity of the model results to a twofold increase in H escape rates is discussed in Section 4.

Having established the effect of O_2 on H escape under Earth-like XUV and UV conditions, we now explore a wider range of stellar fluxes. Figure 7 shows the results of simulations where we varied stellar XUV and UV separately over four orders of magnitude. For both XUV and UV, we use axes scaled to Earth's present-day averaged fluxes ($F_{XUV,0} = 4 \times 10^{-3}$ W m^{-2} and $F_{UV,0} = 1.9 \times 10^{12}$ photons cm^{-2} s^{-1}), as calculated by integrating the solar spectrum data of Thuillier et al. (2004). The quantity plotted is the oxidation rate E (see Figure 2) in TO Gyr^{-1}. We calculate this as

$$E = \frac{4\pi r_P^2 t_{Gy}}{N_{e,TO}} \Phi_H, \qquad (25)$$

where Φ_H is the number flux in question ($\Phi_{H,E}$, $\Phi_{H,\mathrm{diff}}$, or $\Phi_{H,UV}$) and t_{Gy} is the number of seconds in 1 Gyr. Figures 7(a) and (b) show the XUV energy and photolysis limits on escape we have already discussed. The XUV energy limit is a linear function of F_{XUV} only, while the photolysis limit is a linear function of both F_{XUV} and F_{UV}. Figure 7(c) shows the actual diffusion-limited H escape rate obtained from the one-dimensional photochemical model.

Figure 7(e) shows the actual H escape rate, which we obtain by combining all three limits. As has been suggested in earlier work (Wordsworth & Pierrehumbert 2013; Schaefer et al. 2016), we find that the photolysis limit is never reached in practice. Instead, XUV energy-limited escape transitions to H diffusion-limited escape at F_{XUV} levels between around 10 and 30 times present-day Earth. The maximum oxidation rate obtained in the 100% pure H_2O atmosphere is around 10 TO Gyr^{-1}. In similar simulations performed with a 10% H_2O, 90% O_2 atmosphere (not shown), the maximum escape rate was approximately 1 TO Gyr^{-1}, confirming that the quasi-linear dependence of $\Phi_{H,\mathrm{diff}}$ on x_{O_2} seen in Figure 6 holds across the range of stellar fluxes studied. Figure 7(f) is the same as Figure 7(e) but for a 10 M_E super-Earth. As can be seen, escape is energy-limited over a wider range of fluxes in this case,
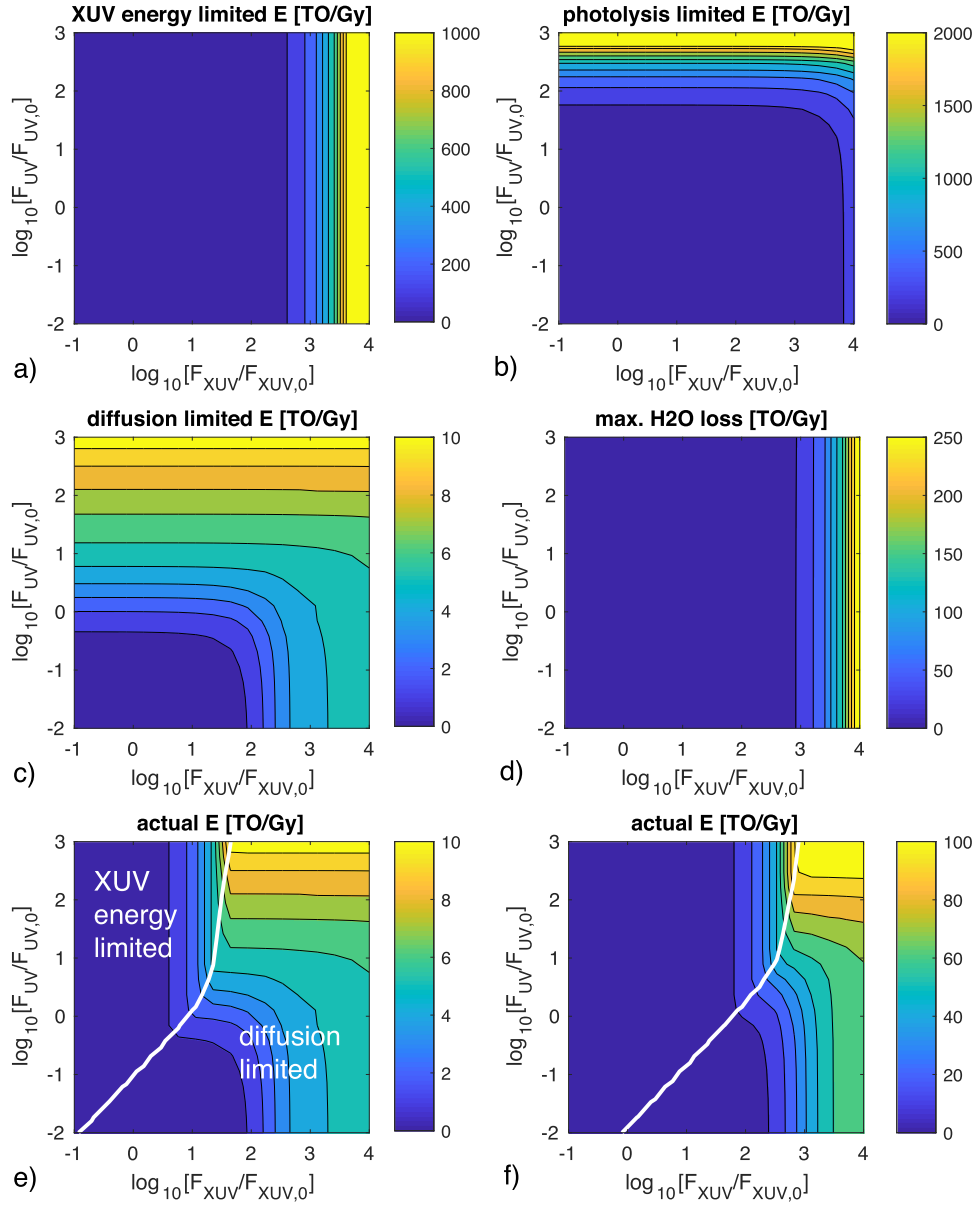
Figure 7. Escape rates as a function of XUV and UV stellar fluxes incident at the top of the atmosphere. Plots (a)–(c) show atomic H escape rate (E) from a 100% H_2O atmosphere assuming that the limiting factor on escape is (a) the supply of XUV energy to power escape (Equation (7)), (b) the rate of supply of UV and XUV photons (Equation (20)), or (c) the upward diffusion of H through the homopause (Equation (13)). Panel (d) shows the H_2O loss rate assuming that excess XUV energy is used to power O escape. Panel (e) shows the actual escape rate of H obtained by combining the limits in panels (b) and (c), with divisions between the regimes indicated by the white line. Panel (f) shows the same thing for a 10 M_E super-Earth.

because the higher super-Earth gravity makes interspecies diffusion much more effective.

We have also performed photochemical simulations with diffusion-limited escape of O, H_2, and OH included and found that this has little effect on the diffusion-limited H escape rate. The H_2 and OH are not abundant enough at the top of the atmosphere in the simulations to affect redox evolution significantly when they escape. Oxygen is a major atmospheric species at high UV and XUV levels, but its diffusion through O_2 and H_2O does not appear to strongly affect the H diffusion rate.

The peak values of E in Figure 7 are close to the maximum rate at which the planet can oxidize via H loss, because if O is effectively dragged along with the H atoms, this will make the escaping gas more oxidizing and hence counteract increases in E. Indeed, for the idealized case of pure escaping H (species 1)

and O (species 2) with $x_1 = x_H = 2/3$, $x_2 = x_O = 1/3$, $m_1 = 1$ amu, and $m_2 = 16$ amu, the number flux in Equation (25) becomes

$$\Phi_{\downarrow,2} \approx \frac{5 b m_p g}{k_B T}, \qquad (26)$$

where m_p is the proton mass, g is gravity, k_B is Boltzmann's constant, and T is temperature (see Appendix A). This expression yields $E = 21.6$ TO Gyr^{-1} for Earth with $T = 300$ K, or about twice the maximum value in Figure 7. The difference is mainly due to the lower values of x_H that occur when a full photochemical calculation is performed, because some liberated H is always mixed downward into the lower atmosphere.

While escape of O along with H cannot significantly alter E, it will still contribute to the overall rate of water (H_2O) loss. Water loss is important both from a habitability perspective and because it plays a key role in regulating a planet's magma ocean phase (next section). The lower limit on H_2O loss is simply the value of E in Figure 7. The upper limit can be estimated by assuming that O also escapes, in the diffusion-limited regime, at a rate determined by the excess XUV energy available to power escape. This loss rate is shown in Figure 7(d). As can be seen, loss rates of tens of TO Gyr^{-1} are theoretically possible at the highest XUV fluxes studied.

To summarize, the key conclusions of this subsection are (a) the rate of planetary oxidation via H_2O photolysis and H escape E is either XUV energy-limited or diffusion-limited, depending on the relative XUV and UV fluxes, and (b) the decrease in the diffusion-limited H escape rate as the O_2 abundance increases is approximately linear.

3.2. Escape Efficiency

Having assessed the role of photolysis and diffusion in the transport of H to the base of the hydrodynamic escape region, we now analyze the efficiency of the escape process itself. The energy-limited hydrodynamic escape (Equation (7)) is useful because of its extreme simplicity. This simplicity comes at a cost: all information on conduction and radiative transfer is subsumed into the efficiency factor ($\equiv$fudge factor) ϵ. Because of the range of processes we are already incorporating in this study, we leave development of a rigorous model of multi-species hydrodynamic escape to future work. However, we can still understand the range of possibilities for H escape by studying limiting cases for the behavior of ϵ as a function of time.

Physically, we should expect that radiative processes will be more important (and hence ϵ will be lower) in situations where (a) more radiating species are present or (b) temperatures are high enough to make new types of emission effective. For pure hydrogen, previous work on hot Jupiters has shown that the main sources of radiation are Lyα radiative cooling and vibrational transitions of the H_3^+ molecule (e.g., Yelle 2004; Murray-Clay et al. 2009). Lyα cooling begins to dominate at escape temperatures around 10^4 K, which is above the blowoff temperature[10] on terrestrial-mass planets for a pure atomic H flow but not when both O and H escape. The H_3^+ emission is important only in atmospheres where H_2 is already abundant. The role of heavier ions in the radiative transfer of an escaping flow is still poorly understood. However, both non-local thermal equilibrium (NLTE) emission from the vibration-rotation bands of molecules such as CO_2 and electronic transitions associated with N, O, and C ions (airglow) are likely to be important.

Here we study three scenarios for ϵ. In the first (ϵ_1), we assume that ϵ maintains a constant high value of 0.3 at all XUV fluxes. In the second (ϵ_2), we assume that $\epsilon = 0.15$ at low XUV levels,[11] but when XUV is high, radiative effects act to cool the flow.

---

[10] Blowoff occurs when the atmospheric scale height approaches the planet radius, or $T \approx r_p m_p g / k_B$ for an H-dominated flow.

[11] In Owen & Mohanty (2016), it is argued that because at low XUV levels the exobase on low-mass planets will be below the sonic point, escape will proceed extremely slowly, at the Jeans limit, and little hydrogen will be lost. However, Johnson et al. (2013), who performed sophisticated Monte Carlo simulations that relaxed the continuum fluid assumption, showed that energy-limited escape is not dependent on the flow becoming supersonic below the exobase, so this outcome is unlikely to be valid in reality.

Specifically, we assume that once O atoms begin to be dragged with the escaping H, they cool the flow so effectively that ϕ is never allowed to increase above ϕ_c (see Equation (12)). In essence, this leads to close to the same limit as the diffusion-limited H escape in Figure 7. Here ϕ_c is calculated using the binary diffusion coefficient for O and H in Table 2 and a homopause temperature of 300 K. Because $\Phi_{\downarrow,2} \propto b/T = T^{-0.25}$, the sensitivity of our results to the assumed homopause temperature is very low.

For the third case (ϵ_3), we allow O escape to occur and assume that radiative cooling by O is not effective, but we allow for Lyα cooling by H atoms. We account for the fact that O drag strongly decreases the scale height of the escaping flow, which means it must heat much more before effective hydrodynamic escape occurs. At these higher temperatures, Lyα cooling of the H could potentially become important. We represent the Lyα cooling limit in a simple way by approximating the escaping wind as isothermal and the density structure as hydrostatic, following Murray-Clay et al. (2009). We write the escape flux as $\phi = \rho_t c_t$, where ρ_t and c_t are the density and sound speed at the transonic point, respectively. Assuming $T = 10^4$ K, $c_t \approx \sqrt{2 \times 10^4 k_B / \overline{m}}$, where $\overline{m}$ is the mean atomic mass of the neutral flow and the factor of two accounts for ionization of all H to H^+ and O to O^+. We neglect higher ionization states than O^+.

From the transonic rule, the transonic point radius is $r_t = GM_P / 2c_t^2$ (Pierrehumbert 2011b). If we assume that ionization occurs rapidly near the base of the flow, hydrostatic balance in spherical coordinates allows us to write

$$\rho_t \approx \overline{m} n_{+,\text{base}} e^{2(1 - r_t/r_p)}, \qquad (27)$$

where $n_{+,\text{base}}$ is the number density of H ions at the base. Finally, assuming that the density at the point of peak XUV absorption is determined by ionization equilibrium, we can balance photoionization and radiative recombination to find

$$n_{+,\text{base}} \approx \sqrt{\frac{F_{\text{XUV}}}{h\nu_0 H_s \alpha_R}}. \qquad (28)$$

Here $h\nu_0 \approx 20$ eV is the mean energy required for one photoionization and $\alpha_R = 2.7 \times 10^{-13} (T/10^4)^{-0.9}$ cm^{-3} atom^{-1} s^{-1} is the hydrogen Case B radiative recombination coefficient (Spitzer 2008). The radiative escape efficiency limit is then calculated as $\epsilon_{\text{Ly}\alpha} = 4V_{\text{pot}}\phi / F_{\text{XUV}}$. To complete our prescription of ϵ_3, we assume that it is never greater than 0.15 or less than ϵ_2, such that

$$\epsilon_3 = \begin{cases} \epsilon_2 & : \quad \epsilon_{\text{Ly}\alpha} \leqslant \epsilon_2 \\ \epsilon_{\text{Ly}\alpha} & : \quad \epsilon_2 < \epsilon_{\text{Ly}\alpha} < 0.15 \\ 0.15 & : \quad \epsilon_{\text{Ly}\alpha} \geqslant 0.15. \end{cases} \qquad (29)$$

These three cases for ϵ are plotted in Figure 8 as a function of F_{XUV} for three terrestrial-mass planets. For Earth, ϵ_2 decreases rapidly after around 100 times the present-day XUV level, while ϵ_3 does not decline until a flux of around $10^4 F_{\text{XUV},0}$ is reached. For the lower-density[12] TRAPPIST-1d, ϵ_2 is lower because O drag commences sooner. Finally, for the super-Earth LHS1140b, the higher gravity enhances diffusive separation of

---

[12] Throughout this paper, we use the reported mass and radius values for all exoplanets. For the TRAPPIST planets and LHS1140b, in particular, the uncertainties in these values should be borne in mind when interpreting the results.
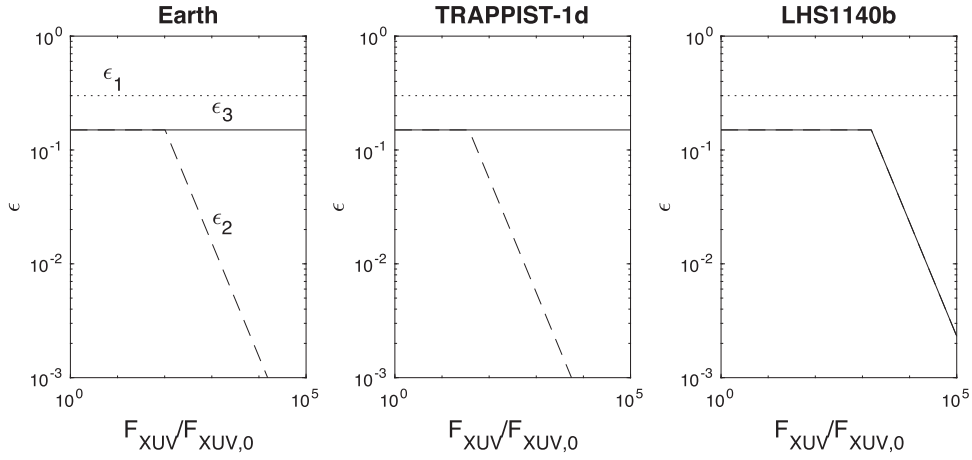
Figure 8. Plot of the escape efficiency ϵ as a function of the incoming XUV flux for Earth ($M_p = M_E$, $r_p = r_E$), TRAPPIST-1d (nominal $M_p = 0.41 M_E$, $r_p = 0.772 r_E$), and LHS1140b ($M_p = 6.65 M_E$, $r_p = 1.43 r_E$). Here $F_{XUV,0} = 4.0 \times 10^{-3}$ W m^{-2} is Earth's present-day received XUV flux. The dotted, dashed, and solid lines correspond to ϵ_1, ϵ_2, and ϵ_3 as described in the text.

O and H and increases the XUV flux required for O drag to commence to around $2 \times 10^3 F_{XUV,0}$. However, the higher gravity also means very high flow temperatures are required for rapid escape once O drag does commence. Hence, in our simple model, Lyα cooling in the mixed H-O flow is predicted to be so efficient that $\epsilon_2 = \epsilon_3$ for all F_{XUV}. Based on this analysis, we choose to treat ϵ_1 and ϵ_2 as upper and lower limits on escape efficiency and ignore the complication of implementing Lyα cooling directly in our coupled model.

In general, hydrodynamic escape should always become more affected by radiative cooling as the planet mass or the mean molar mass of the flow increases. Effective escape requires the upper atmosphere to be heated until its scale height starts to approach the planetary radius, and this requires much higher temperatures when the planet is massive or the escaping species is heavier than pure H. But higher temperatures frequently lead to more efficient radiative processes, which steal energy that could otherwise be used to power escape.

3.3. Total Potential Oxidation Rates

We now summarize the results of this section by calculating the atmospheric oxidation that would occur over a planet's history if the rate of exchange with the surface was zero ($k_1 = k_2 = 0$) and H_2O was always abundant in the planet's upper atmosphere. For Venus, Earth, and Mars, as well as a range of recently discovered low-mass exoplanets, we use Equations (7)–(29) to calculate the integrated change in oxidation state of the volatile layer:

$$N_a(t_1) = \int_{t_0}^{t_1} \frac{dN_a}{dt} dt = \int_{t_0}^{t_1} E \, dt. \qquad (30)$$

The integration is performed starting from 10 My after the host star's formation and assuming $N_a(t_0) = 0$. To derive upper and approximate lower limits on E, we take $t_1 = 5$ Gy and $t_1 = 100$ My, respectively. We also incorporate limits on escape due to both the diffusion rate and the escape efficiency. The dependence of E on O_2 buildup is neglected for now (this assumption is relaxed in the next section). We model the changing stellar luminosity L using the data of Baraffe et al. (2015) and make similar assumptions on XUV evolution as in Schaefer et al. (2016). Specifically, we assume an upper limit
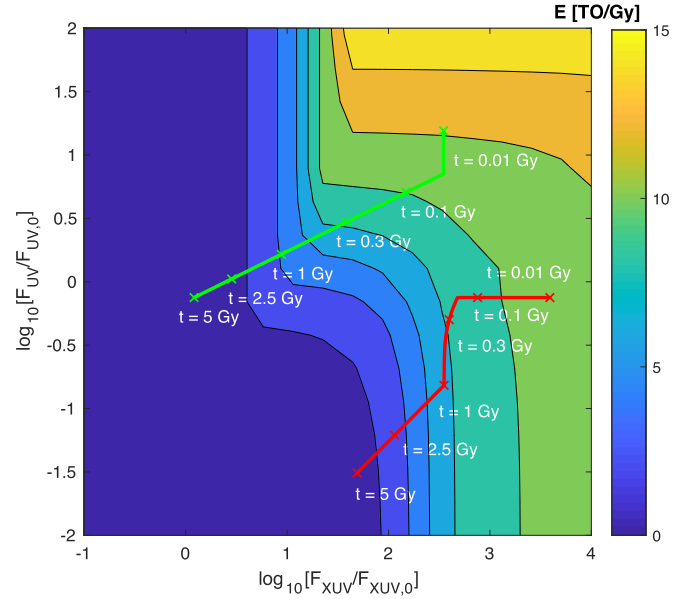

Figure 9. Tracks showing modeled stellar XUV and UV evolution vs. time. The green line shows the Sun, while the red line shows Proxima Centauri for XUV model A. The Proxima data is scaled to represent a planet receiving a bolometric flux of 1366 W m^{-2} at 5 Gyr. For context, the contour plot of the H escape rate as a function of stellar XUV and UV (Figure 7(e)) is shown in the background.

for XUV (model A) where $L_{XUV} = 10^{-3} L$ for a set interval t_{sat}, then follows the power law $L_{XUV} = 10^{-3} (t/t_{sat})^{-1.23} L$ (Ribas et al. 2005) thereafter. We set $t_{sat} = 50$ My for the Sun and $t_{sat} = 1$ Gy for M-class stars. We assume a lower limit (model B) where $L_{XUV} = 10^{-3} L(t_1)$, then drops immediately to zero afterward. Figure 9 shows G- and M-star evolutionary tracks versus F_{XUV} and F_{UV}, with the same plot of E as in Figure 7(e) also shown for reference.

To derive upper and lower limits on oxidation, we combine XUV model A with escape efficiency ϵ_1 and XUV model B with escape efficiency ϵ_2, as described in the last subsection. For the TRAPPIST-1 planets, as a lower limit on XUV, we use a constant $L_{XUV} = 1.2 \times 10^{20}$ W, based on recent *XMM-Newton* X-ray observations of the host star (Wheatley et al. 2017). Note that this XUV flux is considerably higher
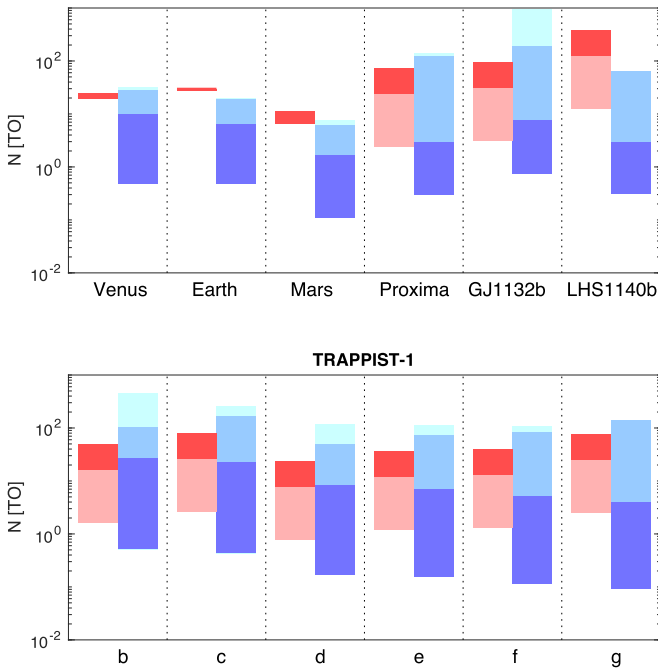
Figure 10. (Top) Comparison between total potential oxidation of the volatile layer (blue) and reducing power (initial FeO content) of the silicate layer (red) for Venus, Earth, Mars, Proxima, GJ1132b, and LHS1140b. (Bottom) Same as top panel but for the TRAPPIST-1b to g planets. Dark blue shows the potential oxidation from H loss assuming diffusion and XUV energy-limited H escape vs. time as in Figure 9, with upper and lower bounds corresponding to $t_1 = 5$ Gy and 100 My, respectively. The peak of the medium blue gives an upper limit on oxidation, with $t_1 = 5$ Gy, $\epsilon = 0.3$, and O escape modeled according to Equation (10). The peak of the light blue shows the total amount of H_2O lost under the same upper-limit assumptions. Dark and light red show the standard and extreme limits on mantle FeO, respectively. Mantle mass fractions and FeO content ranges for Earth, Venus, and Mars are taken from McDonough & Sun (1995), Righter & Drake (1996), Javoy (1999), and Robinson & Taylor (2001).

than the value assumed in Bolmont et al. (2016), which was published before direct X-ray observations of the star were available. All data on exoplanet mass, radius, and orbit and their host star luminosities is taken from the relevant discovery papers (Berta-Thompson et al. 2015; Dittmann et al. 2017; Gillon et al. 2017).

For the UV part of the spectrum, for the Sun, we scale the spectrum based on the parameterization of Claire et al. (2012). For the M-star exoplanets, we scale the XUV and UV portions using the synthetic spectrum for GJ832 from the MUSCLES database (Loyd et al. 2016), which is designed to be a proxy for Proxima Centauri. To incorporate UV time evolution, we incorporate the empirical time dependence formulae proposed by Shkolnik & Barman (2014), with a saturation point at 200 My age at 30 times the baseline UV value. For simplicity, we also use this formulation for the TRAPPIST planets, although we note that the UV evolution of very low-mass M stars is still extremely uncertain. We incorporate the results in escape from the previous two subsections by assuming that once the XUV energy-limited escape rate (Equation (7)) becomes greater than the diffusion limit $\Phi_{H,diff}$, the latter sets the total H escape rate.

In Figure 10, limits on the potential oxidation $N_a(t_1)$ from hydrogen escape are shown in blue alongside estimates of the mantle-reducing potential $|N_b(t_0)|$ in red, which we take to be equivalent to the initial FeO content here. Light blue shows the extreme upper limit on the total water (H_2O) lost via H escape

to space, which is larger than the upper limit on $N_a(t_1)$ in situations where escape of oxygen with escape of H is significant. On the exoplanet plots, a mantle FeO content range of 5–15 wt% is assumed for the dark red bars, and the mantle mass fraction is set to 0.7. The light red denotes an "extreme lower-limit" mantle FeO content of 0.5 wt%, corresponding to values seen in some silicates on Mercury (Zolotov et al. 2013). As can be seen, the variation among the cases is significant, with $N_a(t_1)$ estimates varying from ~0.1 to >100 TO, while the $|N_b(t_0)|$ estimates range from 10 to hundreds of TO.

The most striking aspect of Figure 10 is that the potential mantle-reducing power is comparable to or much greater than the potential oxidation $N_a(t_1)$ for many of the cases. It is also much greater than the conservative estimate of $N_a(t_1)$ (dark blue) in all cases. For all exoplanets except LHS1140b and TRAPPIST-1g, the extreme upper limit on total water loss is greater than $N_a(t_1)$. This is due to the fact that their high early XUV and relatively low UV keeps escape in the diffusion-limited regime (Figure 9). All cases exhibit total potential water loss of more than 1 TO for $t_1 = 5$ Gy, although we stress that this assumes water never becomes cold-trapped on the planet's surface. The huge reducing power of planetary mantles highlights the importance of performing coupled simulations of atmosphere–interior evolution, which we address next.

4. Atmosphere–interior Exchange: The Magma Ocean Phase

To assess when XUV-driven H escape will actually drive N_a to positive values and hence cause abiotic O_2 buildup, we now relax our assumption that $k_{1,2} = 0$ and turn to coupled atmosphere–interior simulations. Rocky planet evolution can be divided into an early period, when the planet's silicate mantle is intermittently or permanently molten, and a much longer subsequent period once the mantle has solidified. Here we use a similar approach to modeling the early magma ocean phase as in Schaefer et al. (2016), with a few important modifications.

First, we determine the interior structure of the planet as a function of its mass. Following Zeng & Sasselov (2013), we solve equations for interior radius r and pressure p versus mass m,

$$\frac{dr}{dm} = \frac{1}{4\pi\rho r^2}, \tag{31}$$

$$\frac{dp}{dm} = -\frac{Gm}{4\pi r^4}. \tag{32}$$

Here G is the gravitational constant and ρ is density. The equations are integrated from the core outward until zero pressure is reached, and Newton's method is then used to find the correct core pressure for a given planetary mass. For the equation of state (EOS), we use a second-order Birch–Murnaghan equation with mantle and core coefficients determined from Earth data (Dziewonski & Anderson 1981; Zeng et al. 2016). This equation reproduces the mass–radius relationships of Earth, Venus, and several low-mass exoplanets within observational error. It requires a value for the core mass fraction f_c, which we take to be 0.3 here. Sensitivity tests indicate a low dependence of the results on the value of f_c over a range of tens of percent.

By neglecting the dependence of interior pressure on temperature [$p = p(\rho)$ only], we greatly simplify our evolution calculations. The mantle temperature profile is calculated from the surface downward as

$$\frac{\partial T}{\partial p} = \frac{\alpha T}{\rho c_{p,m}},\qquad(33)$$

where α, the thermal expansivity, is determined as in Abe (1997) and $c_{p,m}$, the mantle specific heat capacity, is taken to be $1000\ \mathrm{J\,kg^{-1}\,K^{-1}}$. Our approach neglects moist adiabat effects (Abe 1997), which leads us to slightly underestimate the mantle melt fraction and hence overestimate magma ocean phase atmospheric O_2 buildup.

We calculate the local melt fraction by mass in the interior as

$$\psi(r) = \begin{cases} 0 & : T \leqslant T_{\mathrm{sol}} \\ \dfrac{T - T_{\mathrm{sol}}}{T_{\mathrm{liq}} - T_{\mathrm{sol}}} & : T_{\mathrm{sol}} < T < T_{\mathrm{liq}}, \\ 1 & : T \geqslant T_{\mathrm{liq}}. \end{cases}\qquad(34)$$

where T_{sol} and T_{liq} are the solidus and liquidus temperature, respectively, which we determine using an extrapolation of the data of Hirschmann (2000) as in Schaefer et al. (2016). In real melts, the variation of ψ with temperature is not as simple as represented by Equation (34), but the difference is not significant for our purposes (for an insightful discussion of this issue, see Miller et al. 1991). We also make the standard assumption that the magma transitions to a high-viscosity mush at a critical ψ value, which we take to be 0.4 here, and assume that the mush has no further contact with the liquid magma for the purposes of chemical equilibration (Lebrun et al. 2013).

We calculate the total silicate layer melt fraction Ψ as a function of surface temperature T_s by numerically integrating Equation (34) in r from the core–mantle boundary to the surface and normalizing to get

$$\Psi(T_s) = \frac{\int_{m(r_c)}^{m(r_p)} \psi(r)\,dm}{(1 - f_c)M_p}.\qquad(35)$$

In our numerical model, $\Psi(T_s)$ is precalculated on a grid of T_s values for a given planet mass, and the result at any T_s is obtained when needed by interpolation. To perform an analytical check on our results (see Appendix B), we have also parameterized it as

$$\Psi = \frac{1}{2}\left(\mathrm{erf}\left[\frac{T_s - T_t}{\Delta T}\right] + 1\right),\qquad(36)$$

where the parameters T_t and ΔT are determined according to a least-squares fit.

The total melt fraction Ψ is shown as a function of surface temperature for 1 and 10 M_E planets in Figure 11. At a very high surface temperature, the base of the magma ocean is deep, and the error associated with our extrapolation of the Hirschmann (2000) solidus data is likely significant. However, the lower T_s range where Ψ varies rapidly is the most important to atmospheric redox evolution. The total melt fraction is much smaller at a given surface temperature for more massive planets because their internal pressure increases more rapidly with depth.
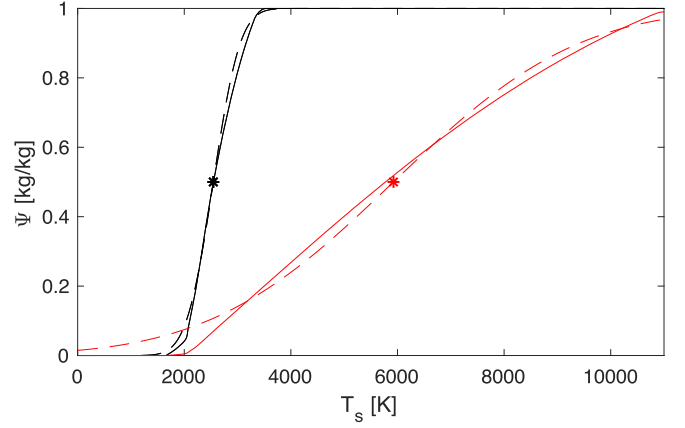

Figure 11. Plot of global mantle melt fraction as a function of surface temperature for a 1 M_E planet (black) and a 10 M_E super-Earth (red). Solid and dashed lines show the numerical integration and least-squares fit of the results according to Equation (36), respectively. Asterisks show the surface temperature T_t at which the global melt fraction is equal to 1/2 the mantle mass.

The atmospheric thermal blanketing (greenhouse effect) is calculated using our line-by-line (LBL) climate model (Schaefer et al. 2016; Wordsworth 2016b; Wordsworth et al. 2017). The 2010 HITEMP line list is used to calculate opacities as a function of pressure, temperature, and wavenumber. In keeping with our aim of calculating approximate upper limits on planetary oxidation, we consider only weakly reducing atmospheres dominated by H_2O and CO_2 here. Addition of an H_2 envelope would prevent O_2 buildup until all H_2 was lost to space, decreasing the final amount of atmospheric O_2 in all cases.

Our calculation uses 8000 spectral points from $1\ \mathrm{cm}^{-1}$ to 5 times the Wien peak for a given surface temperature. One hundred layers are used in the vertical, and an isothermal stratosphere at 200 K is assumed. The temperature profile is calculated as a dry adiabat in the lower atmosphere and a moist adiabat, when appropriate, in the higher atmosphere, following the approach of Wordsworth & Pierrehumbert (2013). Specific heat capacity is calculated based on a specific concentration weighted average, with temperature variation accounted for using data from Lide (2000). For H_2O, we use the MT-CKD continuum version 2.5.2, while for CO_2, we use the GBB approach of Wordsworth et al. (2010a; Gruszka & Borysow 1998; Baranov et al. 2004). The CO_2 continuum is not critical to our results, as it is masked by water vapor lines at most temperatures and pressures. We then use the LBL model to produce a grid of outgoing longwave radiation (OLR) values as a function of surface temperature T_s and surface pressure p_s. The nominal planetary albedo A is set to 0.3, although we test the sensitivity of our results to this parameter. Given the uncertainties in cloud processes, we regard this as a better approach for now than performing detailed shortwave calculations.

We solve for the thermal state of the interior versus time using the energy balance at the top of the atmosphere,

$$\mathrm{OLR}(T_s, p_s) = \frac{(1 - A)L(t)}{4\pi d^2}.\qquad(37)$$

Here L is the time-dependent stellar luminosity and d is the planet's semimajor axis. This approach neglects thermal transients due to the latent and sensible heat of the melt,

which is a simpler approach than was taken in Schaefer et al. (2016). Because a key focus here is understanding the pre-main-sequence magma ocean phase of exoplanets around M stars, we neglect the additional heating provided by accretion and radioactive decay. Previous work has shown that long-half-life elements such as U, Th, and K do not alter the magma ocean duration significantly, while short-half-life elements such as ^{26}Al will only be important if both the accretion time and the star's pre-main-sequence phase are short (Lebrun et al. 2013). Stellar luminosity as a function of time is calculated from the Baraffe et al. (2015) stellar evolution model data set.

The solubility of H_2O in silicate melts is high and must be taken into account in any magma ocean model. We relate the surface pressure p_v of H_2O to the mass fraction q_v of H_2O in the melt as

$$\frac{p_v}{p_{ref}} = \left(\frac{q_v}{q_{ref}}\right)^{1/\beta}. \tag{38}$$

Here $p_{ref} = 24.15$ MPa, $q_{ref} = 0.01$ kg kg^{-1}, and $\beta = 0.74$ (Papale 1997; Schaefer et al. 2016). Assuming that the amount of H_2O that becomes trapped in the solid mantle is small, the total H_2O mass equals the mass in the atmosphere M_a plus that in the melt M_v:

$$M_{tot} = M_a + M_v. \tag{39}$$

Noting that $M_{tot} = q_{H_2O}M_p$, $M_a = 4\pi r_p^2 p_v / g$, and using Equation (38), the mass balance between atmosphere and magma ocean can be calculated by solving

$$0 = q_{H_2O}M_p - 4\pi r_p^2 p_v/g - M_p(1 - f_c)\Psi q_{ref}\left(\frac{p_v}{p_{ref}}\right)^\beta \tag{40}$$

as a function of p_v. Equation (40) implies that for an Earth-mass planet with an entirely molten mantle containing 10 TO of H_2O, the total atmospheric H_2O inventory will only be 0.2 TO.

For a given planet, we calculate atmospheric oxidation as a function of the starting H_2O and mantle FeO inventories. We calculate the XUV-driven loss of H_2O versus time using Equations (7)–(10) from Section 3. We account for the effect of O_2 buildup on H escape by assuming a simple linear dependence of $\Phi_{H,diff}$ on x_{O_2}, such that

$$\Phi_{H,diff} = \Phi_{H,diff}|_{x_{O_2}=0}(1 - x_{O_2}). \tag{41}$$

This differs from our representation of the effects of O_2 on H escape in Schaefer et al. (2016), which was based on an analytic formula for diffusion of H in O (Tian 2015). We solve for T_s versus time using a nested root-finding algorithm on Equations (37) and (40) simultaneously. Finally, redox evolution is calculated by noting that because SiO_2, MgO, and Fe_2O_3 have a net oxidizing power of zero in our classification scheme (Table 1), the total oxidizing power of the mantle is simply $N_b = \sum_i N_{b,i}p_i = -N_{FeO}$, which is always less than or equal to zero. The rate of change of oxidizing power in the liquid part of the silicate layer (i.e., the magma ocean) is equal to twice the downward flow of liberated oxygen ($p_O = +2$; see Table 1) from the atmosphere, minus the rate at

which FeO is lost due to mantle solidification,

$$\frac{dN_{b,l}}{dt} = 2\Phi_{\downarrow,2} - N_{b,l}\frac{d\Psi}{dt}. \tag{42}$$

The mixing rates k_1 and k_2 between the magma ocean and atmosphere are assumed to be much smaller than a single model timestep. Conversely, we assume no mixing between the magma ocean and the high-viscosity part of the silicate layer (mush + solid with $\psi > 0.4$). Because magma ocean crystallization begins at depth, the result for a planet that is steadily losing hydrogen is a mantle that becomes more oxidizing at larger radii (see, e.g., Figure 10 in Schaefer et al. 2016). Based on our mantle oxygen fugacity analysis (Section 5), we assume that O_2 begins to accumulate in the atmosphere once the $Fe^{3+}/(Fe^{2+} + Fe^{3+})$ ratio in the magma ocean reaches 0.3 (see Figure 14). Our evolution model is run until the pre-main-sequence water-loss phase finishes, which we assume occurs once the planet's absorbed stellar radiation (ASR) drops below the runaway greenhouse limit determined from the LBL climate data (around 282 W m^{-2} for an Earth-mass planet).

Figure 12 shows the model results for a range of cases as a function of the starting mantle FeO mass fraction and global H_2O mass fraction. The colored contours show the atmospheric O_2 buildup (equivalently, the value of N_a) in TO equivalent units. The red dashed line shows the analytic limit calculated according to Equation (70) in Appendix B. The match with the numerical model is not exact but is close enough to demonstrate that we can correctly reproduce the essence of the model behavior.

The class labels describe the final volatile-layer inventories and correspond to I: pure H_2O, II: $O_2 + H_2O$, and III: pure O_2. Class I planets begin with so much H_2O that they have molten surfaces until the very end of the pre-main-sequence phase and sufficient mantle FeO that all liberated O from the atmosphere is absorbed. Class II planets oxidize their upper mantles but retain some H_2O, leaving them with mixed O_2–H_2O atmospheres. Class III planets lose all of their water to space. As can be seen, in most of the plots, Class I, where little or no O_2 is present, is the dominant evolutionary outcome. This regime may be the appropriate one for many of the TRAPPIST planets, based on recent analysis suggesting they have a water-rich interior composition (Unterborn et al. 2018).

Comparison of Figures 12(a), (c), and (d) shows that pre-main-sequence O_2 buildup is most sensitive to a planet's orbit and albedo. The reason for this is that both parameters strongly affect t_{RG}, the time at which stellar luminosity decreases enough for the planet to exit the runaway greenhouse phase. An increase in the planet's mass (Figure 12(b)) leads to higher peak values of atmospheric O_2 because diffusive separation of O and H is more effective under the higher gravity and the total mantle melt fraction is lower for a given surface temperature. However, the peak values normalized to the planet's mass are lower. The presence of moderate amounts of atmospheric CO_2 (Figure 12(e)) has little effect on the results, in contrast to the situation for planets that are no longer in a runaway greenhouse state (Wordsworth & Pierrehumbert 2013). Figures 12(f) and (g) show results as in panel (a) but allowing O escape according to diffusion limits from the photochemical model (f) and according to Equations (9) and (10) with fixed $x_O = 1/3$ and $x_H = 2/3$ (g). The latter case shows O_2 buildup several times greater than when the results of the 1D photochemical model are incorporated.
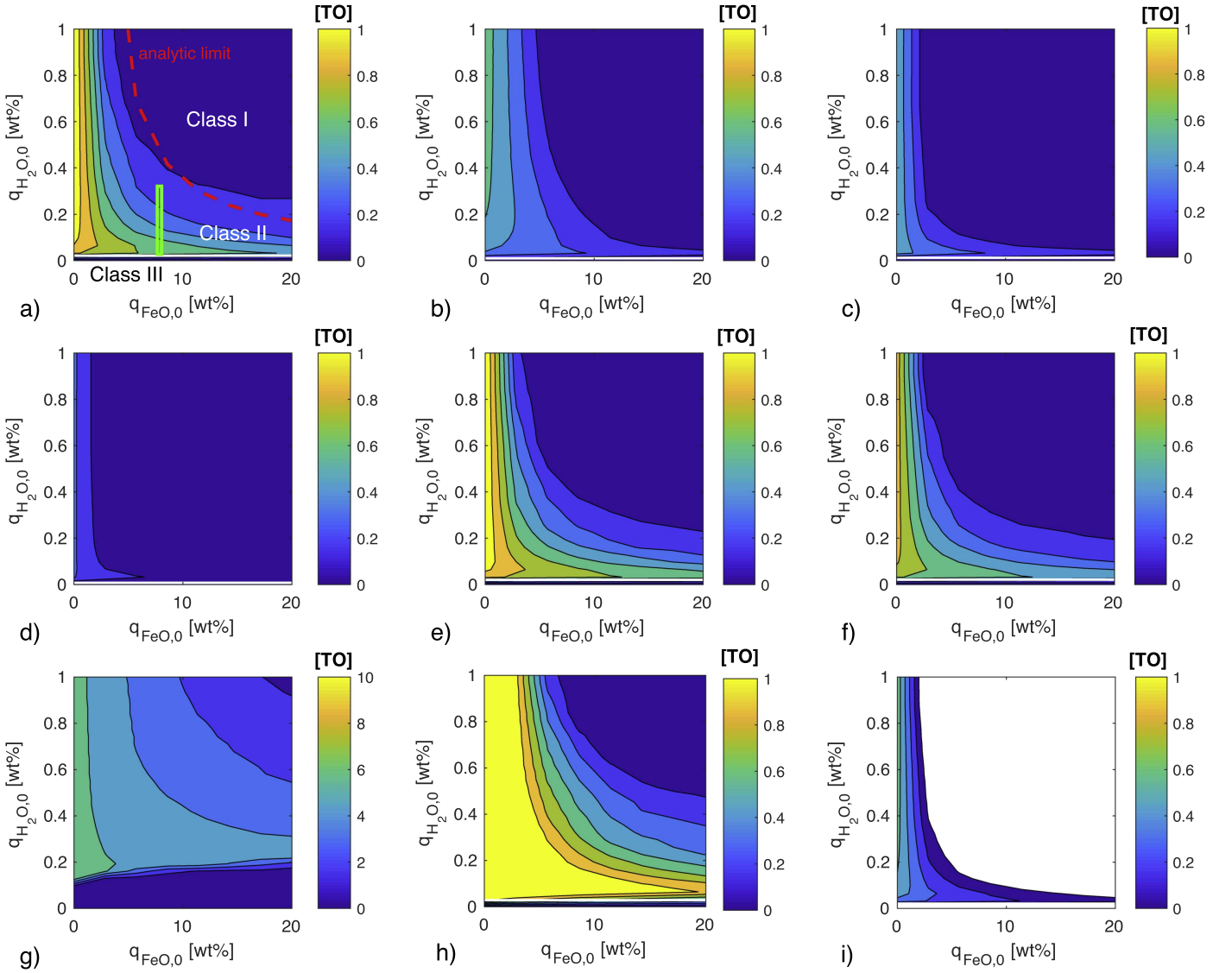
Figure 12. (a)–(g) Contour plots of atmospheric O_2 immediately following the pre-main-sequence runaway greenhouse phase of a planet orbiting an M dwarf. The *x*-axis is the initial specific concentration (weight fraction) of FeO in the mantle, while the *y*-axis is the initial volatile-layer H_2O inventory, expressed as a specific concentration relative to the entire planet mass. In panel (a), the green box bounds the estimated mantle iron and H_2O abundance of Earth, while the red dashed line shows the analytic limit of O_2 buildup given by Equation (70). Panels (b)–(e) are the same as panel (a) but for (b) a 10 M_E super-Earth, (c) a planet receiving the same final stellar flux as Prox Cen (b), (d) a planet with albedo of 0.7, and (e) a planet with 100 bars CO_2 also present in the atmosphere. The contours in (b) are scaled by a factor of 10 to account for the elevated planetary mass. Panels (f) and (g) show escape rates as in panel (a) but assuming that O escape also occurs at a rate determined by the photochemical model (f) or the direct application of the diffusion Equations (9)–(10) with fixed $x_O = 1/3$ and $x_O = 2/3$ (g). Finally, panel (h) is the continuation of panel (a) for 5 Gyr after the pre-main-sequence phase, assuming a loss rate of oxidizing power to the interior of 0.2 TO Gyr^{-1}.

Another effect we considered was the possible differences in atmospheric chemistry due to the presence of species other than O and H. For example, in atmospheres where CO_2 is present, it will also photolyze, and CO and O will be produced as a result (Yung & DeMore 1999). Reactions such as $CO + OH \rightarrow CO2 + H$ could then enhance the stripping of hydrogen from H_2O and hence the H escape rate. We think that processes such as these are unlikely to dominate in the steam-dominated atmospheres we are considering here. However, they could plausibly alter H escape rates by some amount. While we leave detailed analysis of C–H–N–O atmospheres to future work, we can test the sensitivity of our results to such processes by altering the H escape rate by a fixed amount. Figure 12(h) shows the result of such a simulation, where the H escape rate was increased by a factor of two in the diffusion-limited regime. As can be seen, the range of conditions under which O_2

buildup is >1 TO increases, although for high starting H_2O and FeO inventories, buildup is still limited. This indicates that while additional study of the photochemistry in more complex systems is probably warranted, such effects are unlikely to change our basic conclusions.

Figure 13 shows the results of calculations similar to those in Figure 12 as a function of received stellar flux for a Proxima-like host star. This time, O_2 buildup is expressed in terms of the resulting equivalent pressure in the atmosphere in bars. The three lines show results for different planet masses and starting H_2O/FeO mantle inventories. Note that in the high H_2O + FeO super-Earth case, no O_2 built up in the atmosphere at any of the orbital distances studied. The orbital distances required for the planet to receive Earth, Proxima b, and LHS1140b equivalent fluxes are shown by the dotted lines. Clearly, O_2 buildup is a very strong function of planet orbital distance, with more
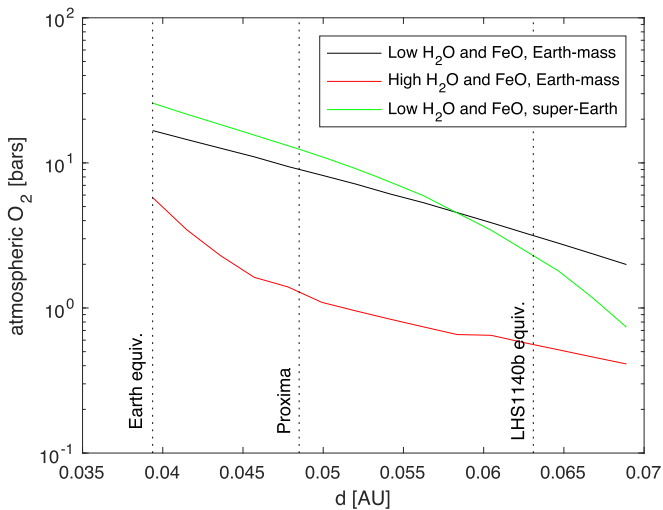
Figure 13. Plots of atmospheric O_2 as a function of orbital distance, immediately following the pre-main-sequence runaway greenhouse phase of a planet orbiting an M dwarf. Colors correspond to an Earth-mass planet with a starting mantle inventory of $q_{FeO} = 0.05$ kg kg^{-1} and $q_{H_2O} = 230$ ppmw (1 TO; black), an Earth-mass planet with a starting inventory of $q_{FeO} = 0.1$ kg kg^{-1} and $q_{H_2O} = 2300$ ppmw (red), and a $10 \times M_E$ super-Earth with a starting inventory of $q_{FeO} = 0.05$ kg kg^{-1} and $q_{H_2O} = 230$ ppmw (1 TO; green).

distant planets far less likely to develop thick O_2 atmospheres. The two key reasons for this are that more distant planets (a) receive fewer XUV photons and (b) have shorter pre-main-sequence runaway greenhouse phases. The implications of this for future observations are discussed in Section 8.

Our results can also be compared with those of Luger & Barnes (2015). That study, which was the first to highlight the importance of the M-star pre-main-sequence phase to exoplanet abiotic O_2, predicted high O_2 buildup but did not incorporate interaction between the atmosphere and interior. For most parameter values, we find significantly lower atmospheric O_2 abundances than were found in Luger & Barnes (2015), demonstrating the importance of atmosphere–interior interactions. It is also important to note that Figures 12(a)–(h) capture an exoplanet's atmospheric state immediately after the magma ocean phase has finished. All of the exoplanets listed in Figure 10 are likely several billion yr old at least. If H escape ceased immediately after their initial runaway greenhouse phases finished, they would evolve to a very different atmospheric state subsequently. The post-runaway phase is studied in more detail next. However, as an example, Figure 12(i) shows the atmospheric O_2 from panel (a) after 5 Gyr has passed, assuming no further H escape (due to, e.g., an effective N_2/CO_2 cold trap) and a constant 0.2 TO Gyr^{-1} loss rate of oxidizing power to the interior. Under these circumstances, the range of cases that continue to have residual atmospheric O_2 from the magma ocean phase becomes very low.

5. Interior–atmosphere Exchange After Mantle Solidification

After a planet cools sufficiently to exit the runaway greenhouse state and the magma ocean freezes, a solid crust forms, and mixing rates between the volatile and silicate layers decrease by orders of magnitude. Once this happens, any subsequent water loss may lead to atmosphere/ocean oxidation

if the rate of redox exchange with the mantle is sufficiently low, even if the total reducing power of the mantle remains high. This period is hence particularly important to the question of abiotic O_2 buildup. Many previous studies have analyzed redox exchange between atmospheric, oceanic, crustal, and mantle reservoirs on Earth and Earth-like planets in some detail (e.g., Holland 2006; Domagal-Goldman et al. 2014; Zahnle & Catling 2014), particularly in the context of the rise of oxygen on Earth (Holland 2006; Laakso & Schrag 2014, 2017). In keeping with the overall approach of this paper, here we constrain the redox budget for a wide range of planetary conditions in a simple way, rather than performing detailed modeling of Earth-specific processes.

Based on the definitions in Table 1, atmospheric O_2 buildup will commence once the volatile-layer oxidizing power N_a becomes positive.[13] From Equation (2), an increasing trend in N_a corresponds to $E - k_1 N_a + k_2 N_b > 0$. This will occur if oxidation via atmospheric loss of hydrogen E outpaces subduction of an oxidized crust and outgassing from a reducing mantle, or if the mantle itself is so oxidized that it can directly outgas O_2.

The outgassing term is proportional to the total rate of volcanism k_2 and the mantle redox state N_b. In general, both terms will be spatially heterogeneous, but we omit this complication here. Assuming a redox budget dominated by H, O, and Fe, a constraint on the H_2O outgassing rate allows the oxidizing power of volcanic gases to be estimated as a function of the mantle redox state, based the equilibrium

$$H_2O \rightleftharpoons H_2 + \frac{1}{2}O_2. \qquad (43)$$
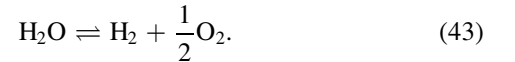
Given an equilibrium constant K_{eq} for Equation (43), we can write an expression for hydrogen molar concentration

$$x_{H_2} = \frac{p_{H_2}}{p_{H_2} + p_{H_2O} + p_{O_2}} \approx \frac{R}{R+1}; \qquad R = \sqrt{\frac{K_{eq}}{f_{O_2}}}. \quad (44)$$

Here f_{O_2} is the oxygen fugacity of the magma (Lindsley 1991), which is the same as the partial pressure p_{O_2} under ideal gas conditions. The second approximate equality in Equation (44) is true as long as $p_{O_2} < p_{H_2O}$. For a typical outgassing temperature ($T = 1450$ K), $K_{eq} = 1.9 \times 10^{-7}$ Pa.[14]

We relate oxygen fugacity f_{O_2} to the iron oxidation ratio of the magma $x_{Fe^{3+}}/x_{Fe_{tot}}$ and temperature T using the empirical formula from Zhang et al. (2017). This formula is based on experimental data from mafic (metal-rich) silicate melts of the type expected for a wide range of volcanic scenarios.[15] Figure 14 shows the results of this calculation. As can be seen, volcanic gases are reducing for $x_{Fe^{3+}}/x_{Fe_{tot}}$ values below around 0.3, i.e., all but the most oxidized magmas. Various

---

[13] Note that our definition of the volatile layer includes both the atmosphere and a liquid H_2O ocean, when present. However, O_2 is relatively insoluble in water, with around 70 TO required on Earth to dissolve 50% of Earth's present-day atmospheric O_2 content (Luger & Barnes 2015). Hence, we treat buildup of O_2 in the volatile layer and the atmosphere as equivalent here.

[14] Our calculation here roughly follows the approach taken in Ramirez et al. (2014). A more complete calculation would account for the pressure dependence of K_{eq}. Analysis of JANAF data shows that K_{eq} increases with pressure, leading to higher rates of H_2 outgassing.

[15] Previous work (e.g., Kress & Carmichael 1991) has shown that the redox state of volcanic gases depends to some extent on the abundance of additional compounds such as Al_2O_3 and MgO. We ignore this extra source of complexity here.
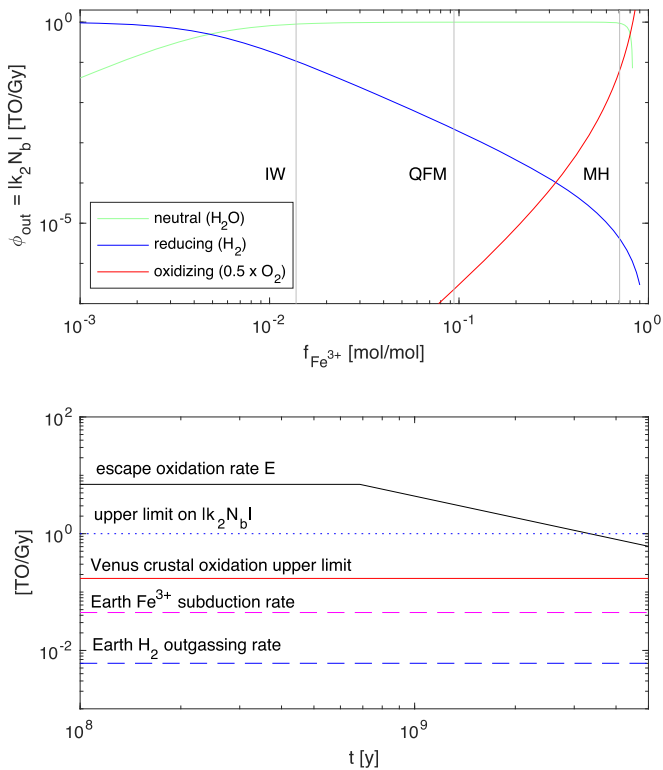
Figure 14. (Top) Volatile-layer redox changes due to volcanic outgassing vs. magma molar ratio of Fe^{3+} to total Fe for a planet with present-day Earth's outgassing rate. The labeled gray lines show several mineral redox buffers (IW = iron-wüstite; QFM = quartz-fayalite-magnetite; MH = magnetite-hematite) based on the data in Lindsley (1991). (Bottom) Volatile-layer redox changes on Earth and Venus due to outgassing and subduction compared with the H escape oxidation rate E for Earth, assuming no cold-trapping. The Venus upper limit is obtained assuming a volcanism rate of 10 km^3 yr^{-1}, with 100% of the magma oxidizing on contact with the atmosphere.

mineral redox buffers are also displayed on the plot. The oxidation state of Earth's upper mantle is close to the quartz-fayalite-magnetite (QFM) buffer (Frost & McCammon 2008), while those of Venus' and Mars' mantles are most likely around magnetite-hematite (MH) and iron-wüstite (IW), respectively (Florensky et al. 1983; Fegley et al. 1997; Wadhwa 2001; Wordsworth 2016a). Clearly, the final Fe^{3+}/Fe ratio of a planet's mantle after its magma ocean phase ceases is critical to its subsequent atmospheric evolution. Planets with Fe^{3+}/Fe $< 5 \times 10^{-3}$ primarily outgas H_2 rather than H_2O, while those with Fe^{3+}/Fe > 0.3 are so oxidizing that they can outgas O_2 directly in significant amounts. Clearly, even if a planet does not build up an O_2 atmosphere from H loss during its magma ocean phase, oxidation of the upper mantle will decrease the reducing power of volcanic gases and hence can facilitate later buildup of an O_2 atmosphere through other mechanisms.

The total rate of volcanism as a function of time on a rocky planet is challenging to calculate from first principles. The extent to which exoplanets can be expected to exist in plate-tectonic, stagnant-lid, or other geodynamical regimes is still a subject of considerable controversy in the literature (e.g., Valencia et al. 2007; Korenaga 2010; Weller & Lenardic 2012). Indeed, in some situations, a strong dependence on initial conditions and hysteresis effects are expected (Weller & Lenardic 2012). Given this, we regard it as wisest to use

constraints from previous modeling and observations of Earth and Venus and do not attempt our own detailed modeling here.

Efficient volcanic outgassing requires (a) a high rate of mantle melting and (b) efficient degassing of the melt once it is close to the surface. Following magma ocean solidification, the primary controls on the mantle melting rate are the mantle temperature and water abundance. Immediately after magma ocean solidification, the mantle will be much hotter than on the present-day Earth. This could potentially lead to a rate of volcanism up to 10–50 times Earth's present-day rate during the first 2 Gyr (Kite et al. 2009). Assuming that this volcanism is associated with the same outgassing rate and composition as on Earth today (1.4×10^{13} mol water yr^{-1}; Parai & Mukho-padhyay 2012), this would result in H_2O outgassing rates of 2–9 TO yr^{-1}. However, degassing of these melts is not assured. Stagnant-lid planets and planets with thick volatile layers (atmosphere or oceans) both suppress degassing from melts due to overburden pressure.[16] Furthermore, hotter mantles may develop more sluggish plate tectonics and thicker crusts due to dehydration of the mantle following melt formation (Kore-naga 2003; Korenaga et al. 2017). We therefore take $|k_2 N_b| \approx 1$ TO Gyr^{-1} as an upper limit on the possible outgassing rate, corresponding to a planet with vigorous plate tectonics and mantle oxygen fugacity around the IW buffer.

For comparison, on present-day Earth (which has plate tectonics), an upper limit on the outgassing rate of H_2O can be taken as 1.8×10^{13} to 1×10^{14} mol yr^{-1}, or 0.23–1.33 TO Gyr^{-1} (Jarrard 2003; van Keken et al. 2011). On Venus, which is currently in a stagnant- or episodic-lid regime, the production rate of crust averaged over geological time is likely around 5 km^3 yr^{-1} based on the atmospheric ^{40}Ar abundance, with an upper limit rate of volcanism from modeling of around 10 km^3 yr^{-1} (Gillmann et al. 2009). All things being equal, this translates to 0.2–2 times Earth's outgassing rate, although Venus' overburden pressure from the 92 bar CO_2 atmosphere likely inhibits H_2O release from magma (Head & Wilson 1986). A crustal oxidation upper limit can be determined using the crustal production rate and the estimated concentration of FeO in the Venusian mantle.

The final important term in the post–magma ocean phase is the rate of removal of oxidizing power from the volatile layer $k_1 N_a$. On planets whose redox balance is dominated by H, O, and Fe, as we are assuming here, the rate of removal of oxidizing power from the atmosphere and crust is primarily determined by the flux of Fe^{3+} to the mantle. This has been estimated for the present-day Earth as 12×10^3 kg s^{-1}, or $k_1 N_a \approx 0.04$ TO Gyr^{-1} (Lécuyer & Ricard 1999). On the early Earth, mantle convection rates were probably higher, which could have resulted in somewhat higher values than this.

Figure 14 plots the limits we have just discussed versus time alongside the maximum oxidation rate via H escape, E, estimated from Figure 7. As can be seen, on many planets, fractions of a TO or more of oxidizing power can be removed from the atmosphere via interior exchange. Hence, in M-star systems older than a few Gyr, only a few planets will retain atmospheric O_2 produced during the pre-main-sequence phase. Nonetheless, the continued hydrogen escape rate is

---

[16] Overburden pressure also has redox implications. For example, a planet with several times Earth's ocean inventory but the same mantle redox state would potentially outgas hydrogen at a significantly lower rate. This could lead to oxidation of the volatile layer via H escape over time even given quite modest rates of H escape. Further modeling is required to assess this possibility quantitatively.

significantly greater than the outgassing and subduction terms under most conditions. Hence, many planets will build up abiotic atmospheric O_2 later in their evolution unless they have an effective cold trap to keep H_2O (and other H-bearing gases) locked in the lower atmosphere. We discuss the cold-trapping process further next.

6. The Key Role of Tropospheric Cold-trapping

In Earth's present-day atmosphere, H_2O is cold-trapped, keeping the stratosphere dry and ensuring that the rate of oxidation is limited by H diffusion through the homopause, rather than the strength of incident UV or XUV stellar radiation. As has been previously demonstrated (Wordsworth & Pierrehumbert 2013, 2014), the partial pressure of noncondensing volatiles (primarily N_2 and O_2) in Earth's atmosphere is critical to the efficiency of this cold trap. If escape of heavy gases is efficient on a given exoplanet, the cold trap will be removed, and hydrogen loss can become rapid again.

A rough guide to the surface N_2/O_2 partial pressure below which cold-trapping ceases to be effective is obtained by setting the moist convection number (Wordsworth & Pierrehumbert 2013)

$$\mathcal{M} = \epsilon p_v L / p_n c_p T_s \tag{45}$$

equal to unity. Here L is the specific latent heat of the condensing gas; c_p is the specific heat capacity at constant pressure of the noncondensing gas (or gas mixture); T_s is temperature; p_v and p_n are, respectively, the partial pressures of the condensing and noncondensing gases in the atmosphere; $\epsilon = m_v/m_n$ is the molar mass ratio between the two gases; and all values are defined at the surface. For a potentially habitable planet with $T_s = 290$ K, $\mathcal{M} = 1$ yields $p_n \approx 0.1$ bar, or around one-eighth of Earth's current atmospheric N_2 inventory.

The atmospheric escape of heavy gases from planets around M stars has recently been studied by several groups. Dong et al. (2017) studied ion escape from Proxima Centauri b powered by stellar wind activity and concluded that several bars of oxygen could have been lost over the planet's lifetime. In addition, Airapetian et al. (2017) modeled the XUV-driven nonthermal ion escape of oxygen and nitrogen and found that tens to hundreds of bars of these gases could be lost from Earth-like planets, provided that the upper atmosphere was hydrogen-poor. Garcia-Sage et al. (2017) studied H^+ and O^+ escape using a slightly different model and came to similar conclusions as Dong et al. (2017) regarding the overall loss rate. Further modeling to account for the complex radiative processes that can occur in ionized N- and O-rich atmospheres will be useful, but at this time it appears that the loss rates of N_2 from habitable-zone planets around M stars may be rapid in many cases. This means that H loss and abiotic O_2 buildup could occur on many of these planets even if they avoid extreme oxidation during their magma ocean phases. Clearly, methods to detect the partial pressure of N_2 remotely on exoplanets (e.g., Schwieterman et al. 2015) should be considered seriously in future mission planning.

7. Abiotic Oxidation Due to Atmospheric Species Other than H_2O

Cold-trapping is only effective if the volatility of the hydrogen host molecule is low for the given atmospheric thermal structure. For terrestrial-type planets with surface liquid water, this means that H_2, CH_4, H_2S, and NH_3 are all species that can cause planetary oxidation when emitted to the atmosphere in significant quantities. The H_2 emission from volcanic outgassing has already been considered in Section 5. Another possibility for H_2 emission is crustal serpentinization. To occur, this process requires the presence of significant quantities of iron in the crust in an intermediate oxidation state (e.g., as the mineral fayalite, Fe_2SiO_4) in direct contact with liquid water. Based on extrapolation of measurements of terrestrial ophiolites (e.g., Etiope et al. 2013), this could plausibly lead to the loss of fractions of a TO's worth of H_2O, depending on the planet's crustal recycling rate.

Methane is another interesting case. The role of biogenic methane in driving the irreversible oxidation of Earth during the Archean and Proterozoic eras has been studied previously (Catling et al. 2001). Based on coupled ecology-climate-chemistry models of the Archean, it has been estimated that CH_4 levels could have built up to 1000 ppm, enough to drive the oxidation of Earth by up to 0.17 TO Gyr^{-1} (Catling et al. 2001; Kharecha et al. 2005). However, on sterile planets, the steady-state abundance of CH_4 is likely to be orders of magnitude lower than this. One further possibility is CH_4 clathrate formation, which has been hypothesized as an explanation for Titan's atmospheric composition (Tobie et al. 2006) and for past episodic warming on Mars (Wordsworth et al. 2017). For episodically frozen water worlds, clathration leads to particularly interesting possibilities. For example, a frozen planet with low outgassing rates and a minimal cold trap might simultaneously build up atmospheric oxygen and subsurface CH_4 clathrate deposits. If these deposits were later destabilized by external perturbations, transient atmospheres containing both O_2 and CH_4 would result. Because CH_4 reacts quite rapidly with O_2 on geological timescales, these cases are likely to be short-lived. Diffusion of oxidized gases from the atmosphere into subsurface ice might also proceed more rapidly than hydrogen escape in many cases. Nonetheless, detailed modeling of this possibility in future would be interesting.

Finally, ammonia and hydrogen sulfide are present only in trace quantities on the present-day Earth and do not contribute significantly to hydrogen loss. Ammonia is easily photolyzed by UV light and is not likely to be abundant enough to cause significant hydrogen escape on either abiotic or inhabited planets with Earth-like ocean volumes. The extreme chemical stability of the N_2 molecule (e.g., Moses 2013; Wordsworth 2016a) means that scenarios where N acts as an effective shuttle to carry H from surface reservoirs past the cold trap are hard to sustain. Scenarios in which H_2S abundances build up to levels sufficient to drive gross oxidation also seem unlikely, based on upper-limit estimates of outgassing on S-rich planets such as Mars (e.g., Halevy & Head 2014) and the relatively high solubility of sulfur species in H_2O, which generally leads to rapid atmospheric removal via rainout.

8. Discussion

One of the key motivations of this study was to determine the situations in which atmospheric O_2 can be regarded as a biosignature, i.e., a reliable indication of the presence of life. Our results indicate that while the presence of O_2 alone should never be regarded as a "smoking gun," it is far more likely to have a biological origin in some cases than in others. Most

Table 4
Qualitative Summary of the Implications of Our Results for a Range of Nearby Low-mass Exoplanets

Planet	Abiotic O_2 Buildup Potential	Remarks
Prox Cen b	MEDIUM	Low received stellar flux, Earth-like mass
GJ1132b	HIGH	High stellar flux: planet is likely sterile
LHS1140b	LOW	Low stellar flux, high planet mass
TRAPPIST-1b	MEDIUM	High stellar flux: planet is likely sterile
TRAPPIST-1c	MEDIUM	High stellar flux
TRAPPIST-1d	MEDIUM	Moderate stellar flux
TRAPPIST-1e	MEDIUM	Moderate stellar flux
TRAPPIST-1f	LOW	Low stellar flux
TRAPPIST-1g	LOW	Low stellar flux

importantly, planets that orbit further from their host stars will lose less hydrogen and N_2 to space and are likely to have higher mantle FeO content (Robinson & Taylor 2001; Fischer et al. 2017), making them much less likely to build up long-lived abiotic O_2 atmospheres.

We find that the pre-main-sequence phase of M dwarfs can lead to significant water loss, in agreement with previous work (Ramirez & Kaltenegger 2014; Luger & Barnes 2015; Tian & Ida 2015). Our photochemical calculations have shown that the rate of H reaching the upper atmosphere via diffusion is the main limit on oxidation when the stellar UV/XUV ratio is low or O_2 has built up to a high abundance in the atmosphere. However, escape can still be quite rapid even in O_2-rich atmospheres. The presence of a hydrogen corona around an exoplanet is therefore still compatible with an O_2-rich atmosphere.

Interaction of the atmosphere with the planet's interior is critical to understanding whether or not an abiotic O_2 atmosphere will build up. In contrast to Luger & Barnes (2015), we find that for a wide range of habitable-zone planets, pre-main-sequence water loss leads to little or no atmospheric O_2 buildup. The oxygen liberated from H_2O photolysis instead mostly reacts with iron in the mantle, which is molten due to the strong greenhouse effect of the planet's steam atmosphere. However, once the planet has cooled and forms oceans and a crust, redox exchange rates between the atmosphere and interior decrease by orders of magnitude, and if the planet lacks a cold trap, hydrogen loss can still lead to abiotic O_2 buildup in many cases (Wordsworth & Pierrehumbert 2014). The issue of how efficiently habitable-zone planets lose "noncondensing" species such as N_2 and CO_2 to space or their interiors is therefore critical to planetary redox evolution, and future observational planning should emphasize ways to constrain the atmospheric abundance of these species.

Planetary oxidation is vital not only to biosignature analysis but also to the question of whether life can originate on a given planet in the first place. Hyper-oxidized planets are likely to be poor places for life to begin, as are planets that remain reducing enough to guard a significant hydrogen envelope. The period in which a planet's surface transitions from strongly reducing to oxidizing conditions is likely to be the ideal period for biogenesis (Wordsworth 2012)—particularly if it involves local redox heterogeneity on the surface. The concept of a "Goldilocks zone" for planetary redox is, in our view, as important as the better-studied habitable zone for liquid water (Kasting et al. 1993).

Table 4 gives a qualitative summary of the implications of our results for a range of the lowest-mass exoplanets in the nearest stellar systems currently known. Despite the many uncertainties, we have provided our overall estimate of the abiotic O_2 buildup potential for each planet as a guide for future work. Of the two planets discovered by the MEarth team, GJ1132b is a good candidate for abiotic O_2 buildup, as we have argued in Schaefer et al. (2016), while LHS1140b is much less likely to develop an abiotic oxygen atmosphere due to its greater orbital distance and higher mass. LHS1140b receives about the same flux as Mars, placing it in the nominal N_2–H_2O–CO_2 habitable zone. Detection of an oxygen-rich atmosphere on this planet would hence be extremely exciting, as it would be unlikely to be due to abiotic processes alone.

For the TRAPPIST planets, the same trends of O_2 buildup with orbital distance and planet mass apply as for the other cases. The low observed densities of many of the planets suggest they may have retained a significant volatile component, perhaps as a result of migration, although the uncertainties in these measurements mean no definite conclusions can be made at present. Retention of an H_2 envelope clearly precludes the presence of O_2, while a thick H_2O layer would move the planets towards the 'Class I' regime of Figure 12, where O_2 buildup is also inhibited. Hence, if the TRAPPIST planet densities are confirmed, abiotic oxygen buildup on them appears unlikely, which makes them (like LHS1140b) very interesting future targets for atmospheric characterization.

In this paper, we have placed special emphasis on the redox evolution of exoplanets around M stars, because these are the cases for which observational tests to our model will come first. However, our results are also applicable to exoplanets around other star types. Because planets that orbit G stars receive fewer XUV photons over their lifetimes for a given total stellar flux, they will undergo less total oxidation in the majority of cases. This is clear from Figure 10, which shows lower total potential oxidation for Venus, Earth, and Mars than for the nine exoplanets studied, all of which orbit M-class stars. As Figure 14 shows, abiotic oxygen atmospheres still have the potential to build up on planets around G stars, but the probability is lower for the majority of cases. Given the challenges to biogenesis and biosignature detection that extreme oxidation poses, this general difference between M- and G-star planets motivates the long-term development of missions to study Earth-like exoplanets around Sun-like stars.

9. Future Work

Improvements in our understanding of planetary redox evolution in future will require developments in several key areas. First, further detail in multispecies escape modeling is still required, including chemistry, conduction, diffusion, and

radiative cooling effects. The way in which 3D dynamics affects water loss in the cold-trap regime and the planetary radiation balance also needs further modeling. Regarding interior processes, further experimental constraints at high pressure and temperature are required to understand core–mantle equilibration and Fe redox disproportionation and hence the initial oxidation state of a planet's mantle. Finally, we note that the generalized framework we have proposed in Section 2 can and should be extended to other species, such as carbon and sulfur, in future.

Ultimately, the most powerful constraints on the modeling described here will come from direct observations. Information on atmospheric composition for hot, sterile planets inside the runaway greenhouse limit, such as TRAPPIST-1b and GJ1132b, will be particularly critical, as it will allow testing and calibration of our models in cases where biologically produced oxygen is not possible. The *James Webb Space Telescope*, which launches in late 2018, will have the ability to characterize the atmospheric composition of most of the planets we have modeled here via a combination of thermal emission and transmission spectroscopy (Morley et al. 2017). Combined with chemical modeling, such observations may allow the oxidation state of the atmosphere N_a to be retrieved. Direct detection of atmospheric O_2 itself will be possible via ground-based high-dispersion spectroscopy starting in the early 2020s or by future direct-imaging missions (Snellen et al. 2013; Rodler & López-Morales 2014; Meadows 2017).

Appendix A
Hydrodynamic Escape of a Binary Gas Mixture

Because clear derivations of the equations for the hydrodynamic escape of a gas mixture from first principles are scarce in the literature, we present details of our own derivation here. We begin from the general equation for diffusion in a binary mixture,

$$\boldsymbol{u}_1 - \boldsymbol{u}_2 = -\frac{1}{x_1 x_2}\frac{b}{n}(\boldsymbol{d}_{12} + k_T \nabla \log T), \quad (46)$$

where

$$\boldsymbol{d}_{12} = \nabla x_1 + \frac{n_1 n_2 (m_2 - m_1)}{n\rho}\nabla \log p - \frac{\rho_1 \rho_2}{p\rho}(\boldsymbol{F}_1 - \boldsymbol{F}_2). \quad (47)$$

Here $\boldsymbol{u}_i$, x_i, n_i, ρ_i, and m_i are the relative velocity, molar concentration, number density, mass density, and molecular mass of species i, respectively. In addition, n, ρ, p, and T are the total number density, mass density, pressure, and temperature, respectively. Finally, b is the binary diffusion coefficient between the two species, and k_T is the thermal diffusion ratio. The derivation of Equation (46) from the Maxwell–Boltzmann equation is described in detail in Chapman & Cowling (1970).

The momentum equation for a binary mixture (Chapman & Cowling 1970, Equation (8.21, 4)) is

$$\nabla p = \rho_1 \boldsymbol{F}_1 + \rho_2 \boldsymbol{F}_2 - \rho\frac{D_0 \boldsymbol{u}_0}{Dt}, \quad (48)$$

where $\boldsymbol{u}_0$ is the mass-weighted mean velocity of the flow and D_0 is the corresponding advective operator. We can substitute this expression into Equation (47) and rearrange to get

$$\boldsymbol{d}_{12} = (\nabla p_1 - \rho_1 \boldsymbol{F}_1')/p, \quad (49)$$

where we have defined the acceleration $\boldsymbol{F}_1'$ in the Lagrangian frame following the flow as

$$\boldsymbol{F}_1' \equiv \boldsymbol{F}_1 - \frac{D_0 \boldsymbol{u}_0}{Dt}. \quad (50)$$

Note that we have also used the definition of partial pressure $p_1 = x_1 p$ and total density $\rho = \rho_1 + \rho_2$. Substituting Equation (49) into Equation (46) and assuming variation in the radial direction only, we find

$$w_1 - w_2 = -\frac{1}{x_1 x_2}\frac{b}{n}\left[\frac{1}{p}\left(\frac{dp_1}{dr} - \rho_1 F_1'\right) + k_T \frac{d\log T}{dr}\right], \quad (51)$$

where w_i is the radial velocity component of $\boldsymbol{u}_i$. Using the ideal gas law for each species $p_i = n_i k_B T$ and writing $g' = -F_1'$, we can write

$$w_1 - w_2 = -\frac{b}{n_2}\left[\frac{d\log n_1}{dr} + \frac{m_1 g'}{k_B T} + \left(1 + \frac{k_T}{x_1}\right)\frac{d\log T}{dr}\right]. \quad (52)$$

This equation is the same as Equation (1) in Hunten et al. (1987), except that our acceleration term is $g' = g + D_0 \boldsymbol{u}_0/Dt$. We think that the additional $D_0 \boldsymbol{u}_0/Dt$ term is unlikely to cause order-of-magnitude differences in the results in most cases, although we leave detailed investigation of its importance to future work.

Next, we define the molecule number flux per unit surface area as $\Phi_i = n_i w_i (r/r_s)^2$. We also drop the thermal diffusion term involving $d\log T/dr$, as previous work (Zahnle & Kasting 1986) has shown that it is generally small. Rearranging Equation (52), we find

$$\frac{dn_1}{dr} = \frac{1}{b}\frac{r_s^2}{r^2}(\Phi_2 n_1 - \Phi_1 n_2) - \frac{n_1}{H_1(r)}, \quad (53)$$

and, by symmetry,

$$\frac{dn_2}{dr} = \frac{1}{b}\frac{r_s^2}{r^2}(\Phi_1 n_2 - \Phi_2 n_1) - \frac{n_2}{H_2(r)}, \quad (54)$$

where $H_i(r) = k_B T(r)/m_i g'(r)$ is the local scale height for species i. Summation of Equations (53) and (54) yields an equation for the total number density of the escaping flow,

$$\frac{dn}{dr} = -\frac{n}{\overline{H}(r)}, \quad (55)$$

where $\overline{H}(r) = k_B T(r)/\overline{m} g'(r)$ and $\overline{m} = m_1 x_1 + m_2 x_2$ is the local mean molar mass. Finally, by expressing $d\log x_2/dr$ in terms of n and n_2 and substituting Equations (53) and (54) into
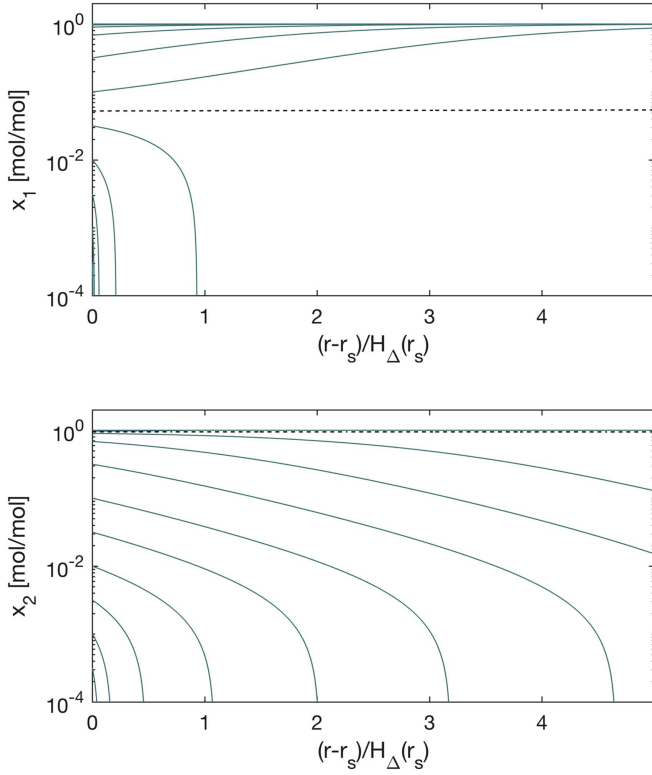
Figure 15. Variation in molar concentration of a light (x_1; top) and heavy (x_2; bottom) escaping species, as determined by numerical integration of Equation (57). Results are shown for an Earth-mass planet, $T = 400$ K, molecular masses and binary diffusion coefficients appropriate for H and O (Table 2), $\Phi_1 = 1 \times 10^{12}$ molecules cm^{-2} s^{-1}, and $\Phi_2 = 0.1\Phi_1$. The various lines show different starting conditions for x_1 at $r = r_s$.

the result, we can derive

$$\frac{d \log x_2}{dr} = \frac{1}{b}\frac{r_s^2}{r^2}[\Phi_1 - \Phi_2(1 - x_2)/x_2]$$
$$+ \frac{g'}{k_B T}(m_1 - m_2)(1 - x_2). \quad (56)$$

Defining $H_\Delta \equiv k_B T/(m_2 - m_1)g'(r)$ and $Y_i \equiv b^{-1}(r_s^2/r^2)H_\Delta \Phi_i$, we can nondimensionalize Equation (56) as

$$H_\Delta \frac{dx_2}{dr} = +x_2^2 + (Y_1 + Y_2 - 1)x_2 - Y_2. \quad (57)$$

Assuming that H_Δ remains finite, local solutions where $dx_2/dr = 0$ are defined by

$$x_2^* = \frac{1}{2}(1 - Y_1 - Y_2 \pm \sqrt{(1 - Y_1 - Y_2)^2 + 4Y_2}). \quad (58)$$

Physical constraints require $0 < x_2(r) \leqslant 1$ for all r, which allows us to discard the solution with the negative square root. In addition, an analytical stability analysis of Equation (57) (not shown here) reveals that the remaining root is in fact an unstable solution. This behavior is seen clearly in Figure 15, which shows the results of numerical integration of Equation (57) in a representative case for a range of starting values. All starting values of x_2 except for one result in either $x_2 \to 0$ or $x_1 \to 0$ at large r, neither of which is consistent with having finite escape fluxes Φ_1 and Φ_2. For isothermal atmospheres where the acceleration correction to g is small, the
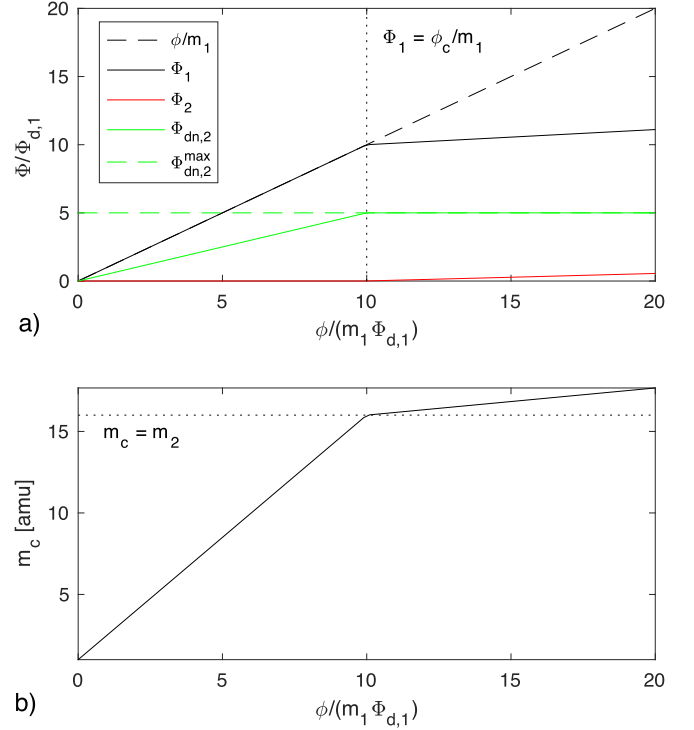

Figure 16. (a) Normalized number fluxes from Equations (9), (10), and (62) and (b) crossover mass from Equation (60) vs. the normalized total mass flux ϕ. Here $m_1 = 1$ amu, $m_2 = 16$ amu, $x_1 = 2/3$, and $x_2 = 1/3$. The dotted line in (a) indicates that drag of species 2 (atomic O) commences when the crossover flux is reached, while (b) shows the equivalent criterion $m_c = m_2$.

correct starting value is simply x_2^*, but in general situations, it can vary, as for the case shown in Figure 15. In realistic flows, both T and g' should increase with altitude, although typically not by enough to change x_2^* by more than a factor of a few.

The key point of Figure 15 is that the cases where x_2 goes to 0 or 1 at large radii are inconsistent with the escape of both species. Only the starting values of x_2 that are close to x_2^* keep $0 < x_2(r) < 1$ for all r. Physically, we can expect that in a temporally evolving flow, the value of x_2 near the base would adjust until this constraint was automatically satisfied.

By mass conservation, the total mass flux must equal the combined mass fluxes of the two species,

$$\phi = m_1 \Phi_1 + m_2 \Phi_2. \quad (59)$$

When the variations of g' and H_Δ with r are small, we can substitute Equation (59) into Equation (58) and rearrange to derive Equations (9) and (10), given Equation (11).

We regard this approach as a significant improvement over the commonly used crossover-mass approach of Hunten et al. (1987), because it starts from first principles, making all approximations clear, and allows us to express the fluxes of species 1 and 2 directly in terms of externally defined quantities. The crossover mass itself can still be used as a diagnostic, as it can be written based on the definition of $\Phi_{d,1}$ as

$$m_c = m_1\left(1 + \frac{\Phi_1}{\Phi_{d,1}x_1}\right). \quad (60)$$

More usefully, the crossover flux ϕ_c defining the threshold for escape of the heavy species 2 is simply equivalent to the value of $\Phi_1 m_1$ when $m_c = m_2$ (see Equation (12) in the main

text). For the water-loss problem, $\phi_c/m_1 = 10\Phi_{d,1}$, or about 1.3×10^{13} atoms cm^{-2} s^{-1} for an Earth-mass planet. For energy-limited XUV-driven escape with efficiency $\epsilon = 0.15$, this requires an XUV flux of around 0.35 W m^{-2}, or around 100 times that incident on Earth today. Figure 16 shows plots of fluxes and the crossover mass versus the species 1 reference flux normalized by its diffusion flux, demonstrating the simplicity of our approach.

Finally, the net buildup of species 2 in the planet's atmosphere can be written in general as

$$\Phi_{\downarrow,2} = \Phi_1(x_2/x_1) - \Phi_2. \quad (61)$$

Hence,

$$\Phi_{\downarrow,2} \approx \begin{cases} (x_2/x_1)\phi/m_1 & : \phi < \phi_c \\ x_2 b(H_2^{-1} - H_1^{-1}) & : \phi \geqslant \phi_c. \end{cases} \quad (62)$$

Given $x_1 = 2/3$, $x_2 = 1/3$, $m_1 = 1$ amu, and $m_2 = 16$ amu, it is easily shown that $\Phi_{\downarrow,2}$ becomes

$$\Phi_{\downarrow,2} \approx \frac{5bm_p g}{k_B T}, \quad (63)$$

in agreement with previous work (Zahnle 1986; Luger & Barnes 2015; Tian 2015).

Appendix B
Analytic Limit on Pre-main-sequence Magma Ocean O_2 Buildup

To ensure that we understand the results of the coupled escape-climate-interior model described in Section 4, here we derive an analytic estimate of the planet composition for which O_2 buildup ceases to occur. First, we parameterize the pre-main-sequence stellar luminosity as

$$L(t) = L_0(t/t_0)^\alpha, \quad (64)$$

where L_0 is the luminosity at time t_0, which we define as the start of the star's main-sequence phase. Based on a least-squares fit of the Baraffe et al. (2015) data, we have found $\alpha = -0.725$, $L_0 = 8.3 \times 10^{-4} L_S$, and $t_0 = 0.43$ Gy for a $0.1 M_S$ red dwarf star.

Next, we assume that O_2 buildup will start to occur when the total oxidation due to preferential H escape is greater than the total amount of FeO in the magma ocean. Rather than performing an integral, we simply estimate the oxidation due to escape as $Et_{RG} = 4\pi r_P^2 t_{RG} \Phi_{H,UV}$, with t_{RG} the time at which the runaway greenhouse state ceases. Hence, the required melt fraction is

$$\Psi_{RG} = \frac{4\pi r_P^2 t_{RG} \Phi_{H,UV}}{f_{Fe_2O_3,max} N_{FeO,0}}. \quad (65)$$

Here $f_{Fe_2O_3,max}$ is the maximum level that Fe_2O_3 is allowed to build up to in the magma, which we take to be 0.3 based on Figure 14. Noting also that $N_{FeO,0} = q_{FeO,0} M_P (1-f_c)/m_{FeO}$, we can use the analytic expression of Equation (36) for Ψ_{RG} and solve for T_s to get

$$T_{s,RG} = T_t + \Delta T \text{erfinv}[2\Psi_{RG} - 1], \quad (66)$$

the minimum surface temperature required at time t_{RG} to avoid H_2O buildup.

The final step is to relate $T_{s,RG}$ to the minimum required starting H_2O inventory. To do this, we first assume that the atmosphere behaves like an optically thick gray emitter (Pierrehumbert 2011b),

$$T_{s,RG} = T_{e,RG}\left(\frac{p_e}{p_{s,RG}}\right)^{R/c_p}, \quad (67)$$

with

$$T_{e,RG} \approx \left(\frac{282 \text{ W m}^{-2}}{\sigma_B}\right)^{1/4}, \quad (68)$$

and $p_e = 0.05$ bar based on comparison with the LBL OLR data. Here R, c_p, and σ_B are the specific gas constant, heat capacity at constant volume, and Stefan–Boltzmann constant, respectively.

The total mass of H_2O required is then the amount lost to space up to time t_{RG}, plus the amount required in the atmosphere and melt required to sustain a surface temperature $T_{s,RG}$, i.e.,

$$M_{H_2O,all} = M_{lost} + M_a + M_v. \quad (69)$$

Equation (69) can be expanded and rearranged as

$$q_{H_2O,0} = \frac{M_{lost}}{M_p} + \frac{4\pi r_p^2 p_{s,RG}}{gM_p} + (1 - f_c)q_{ref}\left(\frac{p_{s,RG}}{p_{ref}}\right)^\beta. \quad (70)$$

Here $p_{s,RG}$ is defined by Equation (67), while M_{lost} is taken from the model results. Despite the number of approximations that have gone into Equation (70), reference to Figure 12 shows that it reproduces the numerical results quite well.

ORCID iDs

L. K. Schaefer ⓘ https://orcid.org/0000-0003-2915-5025

References

Abe, Y. 1997, PEPI, 100, 27
Ahrens, T. J. 1993, AREPS, 21, 525
Airapetian, V. S., Glocer, A., Khazanov, G. V., et al. 2017, ApJL, 836, L3
Anglada-Escudé, G., Amado, P. J., Barnes, J., et al. 2016, Natur, 536, 437
Baraffe, I., Homeier, D., Allard, F., & Chabrier, G. 2015, Astro & Astrophysics, 577, A42
Baranov, Y. I., Lafferty, W. J., & Fraser, G. T. 2004, JMoSp, 228, 432
Barnes, R., Deitrick, R., Luger, R., et al. 2016, arXiv:1608.06919
Berta-Thompson, Z. K., Irwin, J., Charbonneau, D., et al. 2015, NatGe, 527, 204
Bolmont, E., Selsis, F., Owen, J. E., et al. 2016, arXiv:1605.00616
Brion, C. E., Tan, K. H., Van der Wiel, M. J., & Van der Leeuw, P. E. 1979, JESRP, 17, 101
Catalli, K., Shim, S.-H., Prakapenka, V. B., Zhao, J., & Sturhahn, W. 2010, AmMin, 95, 418
Catling, D. C., Zahnle, K. J., & McKay, C. P. 2001, Sci, 293, 839
Chaffin, M. S., Deighan, J., Schneider, N. M., & Stewart, A. I. F. 2017, NatGe, 10, 174
Chan, W. F., Cooper, G., & Brion, C. E. 1992, CP, 168, 375
Chan, W. F., Cooper, G., & Brion, C. E. 1993a, CP, 170, 99
Chan, W. F., Cooper, G., & Brion, C. E. 1993b, CP, 178, 387
Chapman, S., & Cowling, T. G. 1970, The Mathematical Theory of Non-uniform Gases: an Account of the Kinetic Theory of Viscosity, Thermal Conduction and Diffusion in Gases (Cambridge: Cambridge Univ. Press)
Chassefière, E. 1996, JGR, 101, 26039
Claire, M. W., Sheets, J., Cohen, M., et al. 2012, ApJ, 757, 95
Clayton, D. D. 1968, Principles of Stellar Evolution and Nucleosynthesis (Chicage, IL: Univ. Chicago Press)
Dittmann, J. A., Irwin, J. M., Charbonneau, D., et al. 2017, Natur, 544, 333

Domagal-Goldman, S. D., Segura, A., Claire, M. W., Robinson, T. D., & Meadows, V. S. 2014, ApJ, 792, 90
Dong, C., Lingam, M., Ma, Y., & Cohen, O. 2017, ApJL, 837, L26
Dziewonski, A. M., & Anderson, D. L. 1981, PEPI, 25, 297
Etiope, G., Ehlmann, B. L., & Schoell, M. 2013, Icar, 224, 276
Fally, S., Vandaele, A. C., Carleer, M., et al. 2000, JMoSp, 204, 10
Fegley, B., Zolotov, M. Y., & Lodders, K. 1997, Icar, 125, 416
Fei, Y., Van Orman, J., Li, J., et al. 2004, JGRB, 109, B2
Fischer, R. A., Campbell, A. J., & Ciesla, F. J. 2017, E&PSL, 458, 252
Fischer, R. A., Nakajima, Y., Campbell, A. J., et al. 2015, GeCoA, 167, 177
Florensky, C. P., Nikolaeva, O. V., Volkov, V. P., et al. 1983, LPSC, 14, 203
Frost, D. J., Liebske, C., Langenhorst, F., et al. 2004, Natur, 428, 409
Frost, D. J., & McCammon, C. A. 2008, AREPS, 36, 389
Garcia-Sage, K., Glocer, A., Drake, J. J., Gronoff, G., & Cohen, O. 2017, ApJL, 844, L13
Gillmann, C., Chassefière, E., & Lognonné, P. 2009, E&PSL, 286, 503
Gillon, M., Jehin, E., Lederer, S. M., et al. 2016, Natur, 533, 221
Gillon, M., Triaud, A., Demory, B.-O., et al. 2017, Natur, 542, 456
Gruszka, M., & Borysow, A. 1998, MolPh, 93, 1007
Halevy, I., & Head, J. W. 2014, NatGe, 7, 865
Harman, C. E., Schwieterman, E. W., Schottelkotte, J. C., & Kasting, J. F. 2015, ApJ, 812, 137
Head, J. W., & Wilson, L. 1986, JGRB, 91, 9407
Hirschmann, M. M. 2000, GGG, 1, 10
Hirschmann, M. M., & Dasgupta, R. 2009, ChGeo, 262, 4
Hirschmann, M. M., & Withers, A. C. 2008, E&PSL, 270, 147
Holland, H. D. 2006, RSPTB, 361, 903
Huebner, W. F., Keady, J. J., & Lyon, S. P. 1992, Ap&SS, 195, 1
Hunten, D. M., Pepin, R. O., & Walker, J. C. G. 1987, Icar, 69, 532
Jarrard, R. D. 2003, GGG, 4, 5
Javoy, M. 1999, CRASE, 329, 537
Johnson, R. E., Volkov, A. N., & Erwin, J. T. 2013, ApJL, 768, L4
Kaltenegger, L., Selsis, F., Fridlund, M., et al. 2010, AsBio, 10, 89
Kasting, J. F., & Brown, L. L. 1998, The Molecular Origins of Life: Assembling the Pieces of the Puzzle (Cambridge: Cambridge Univ. Press)
Kasting, J. F., & Pollack, J. B. 1983, Icar, 53, 479
Kasting, J. F., Whitmire, D. P., & Reynolds, R. T. 1993, Icar, 101, 108
Kharecha, P., Kasting, J., & Siefert, J. 2005, Geobiology, 3, 53
Kite, E. S., Manga, M., & Gaidos, E. 2009, ApJ, 700, 1732
Kopparapu, R. K., Ramirez, R., Kasting, J. F., et al. 2013, ApJ, 765, 131
Korenaga, J. 2003, GeoRL, 30, 1437
Korenaga, J. 2010, ApJL, 725, L43
Korenaga, J., Planavsky, N. J., & Evans, D. A. 2017, RSPTA, 375, 20150393
Kress, V. C., & Carmichael, I. S. E. 1991, CoMP, 108, 82
Kuramoto, K., & Matsui, T. 1996, JGRE, 101, 14909
Laakso, T. A., & Schrag, D. P. 2014, E&PSL, 388, 81
Laakso, T. A., & Schrag, D. P. 2017, Geobiology, 15, 366
Lammer, H., Kasting, J. F., Chassefière, E., et al. 2008, SSRv, 139, 399
Lebrun, T., Massol, H., Chassefière, E., et al. 2013, JGRE, 118, 1155
Lécuyer, C., & Ricard, Y. 1999, E&PSL, 165, 197
Lenardic, A., & Crowley, J. W. 2012, ApJ, 755, 132
Lide, D. P. (ed.) 2000, CRC Handbook of Chemistry and Physics (81th ed.; Boca Raton, FL: CRC Press)
Lindsley, D. H. 1991, Oxide Minerals: Petrologic and Magnetic Significance, Vol. 25 (Chantilly, VA: Mineralogical Society of America)
Linstrom, P. J., & Mallard, W. G. 2001, J. Chem. Eng. Data, 46, 1059
Lodders, K. 2003, ApJ, 591, 1220
Loyd, R. O. P., France, K., Youngblood, A., et al. 2016, ApJ, 824, 102
Luger, R., & Barnes, R. 2015, AsBio, 15, 119
Marrero, T. R., & Mason, E. A. 1972, Gaseous Diffusion Coefficients (Melville, NY: AIP)
Marty, B. 2012, E&PSL, 313, 56
McDonough, W. F., & Sun, S.-S. 1995, ChGeo, 120, 223
McElroy, M. B., & Donahue, T. M. 1972, Sci, 177, 986
Meadows, V. S. 2017, AsBio, 17, 1022
Meadows, V. S., Arney, G. N., Schwieterman, E. W., et al. 2016, arXiv:1608.08620
Miller, G. H., Stolper, E. M., & Ahrens, T. J. 1991, JGRB, 96, 11849
Miller, S. L., & Urey, H. C. 1959, Sci, 130, 245
Morbidelli, A., Chambers, J., Lunine, J. I., et al. 2000, M&PS, 35, 1309
Morley, C., Kreidberg, L., Rustamkulov, Z., Robinson, T., & Fortney, J. J. 2017, ApJ, 850, 121
Moses, J. I. 2013, arXiv:1307.5450
Moses, J. I., Visscher, C., Fortney, J. J., et al. 2011, ApJ, 737, 15
Mota, R., Parafita, R., Giuliani, A., et al. 2005, CPL, 416, 152
Murray-Clay, R. A., Chiang, E. I., & Murray, N. 2009, ApJ, 693, 23

O'Neill, H. S. C., Berry, A. J., McCammon, C. C., et al. 2006, AmMin, 91, 404
Olney, T. N., Cann, N. M., Cooper, G., & Brion, C. E. 1997, CP, 223, 59
Oparin, A. I. 1938, in The Origin of Life on the Earth, ed. I. Number (New York: The Macmillan Company)
Owen, J. E., & Mohanty, S. 2016, MNRAS, 459, 4088
Papale, P. 1997, CoMP, 126, 237
Parai, R., & Mukhopadhyay, S. 2012, E&PSL, 317, 396
Pauling, L. 1967, The Chemical Bond (Ithaca, New York: Cornell Univ. Press)
Pierrehumbert, R. T. 2011a, ApJL, 726, L8
Pierrehumbert, R. T. 2011b, Principles of Planetary Climate (Cambridge: Cambridge Univ. Press)
Powner, M. W., Gerland, B., & Sutherland, J. D. 2009, Natur, 459, 239
Rafikov, R. R. 2006, ApJ, 648, 666
Ramirez, R. M., & Kaltenegger, L. 2014, ApJL, 797, L25
Ramirez, R. M., Kopparapu, R., Zugger, M. E., et al. 2014, NatGe, 7, 59
Ranjan, S., & Sasselov, D. D. 2017, AsBio, 17, 169
Ribas, I., Guinan, E. F., Güdel, M., & Audard, M. 2005, ApJ, 622, 680
Righter, K., & Drake, M. J. 1996, Icar, 124, 513
Ringwood, A. E. 1959, GeCoA, 15, 257
Robinson, M. S., & Taylor, G. J. 2001, M&PS, 36, 841
Rodler, F., & López-Morales, M. 2014, ApJ, 781, 54
Rubie, D. C., Frost, D. J., Mann, U., et al. 2011, E&PSL, 301, 31
Rubie, D. C., Jacobson, S. A., Morbidelli, A., et al. 2015, Icar, 248, 89
Rubie, D. C., Melosh, H. J., Reid, J. E., Liebske, C., & Righter, K. 2003, E&PSL, 205, 239
Samson, J. A. R., & Haddad, G. N. 1994, JOSAB, 11, 277
Sander, S. P., Friedl, R. R., & Barker, J. R. 2009, Chemical Kinetics and Photochemical data for use in Atmospheric Studies Evaluation Number 16: Supplement to Evaluation 15: Update of Key Reactions, Technical Report, Pasadena, CA: Jet Propulsion Laboratory
Schaefer, L., Wordsworth, R. D., Berta-Thompson, Z., & Sasselov, D. 2016, ApJ, 829, 63
Schwieterman, E. W., Robinson, T. D., Meadows, V. S., Misra, A., & Domagal-Goldman, S. 2015, ApJ, 810, 57
Seager, S., Schrenk, M., & Bains, W. 2012, AsBio, 12, 61
Selsis, F., Despois, D., & Parisot, J.-P. 2002, A&A, 388, 985
Shkolnik, E. L., & Barman, T. S. 2014, AJ, 148, 64
Siebert, J., Badro, J., Antonangeli, D., & Ryerson, F. J. 2012, E&PSL, 321, 189
Snellen, I. A. G., de Kok, R. J., le Poole, R., Brogi, M., & Birkby, J. 2013, ApJ, 764, 182
Solomatov, V. S. 2007, Treatise on Geophysics, Vol. 9 (New York: Elsevier)
Spitzer, L. 2008, Physical Processes in the Interstellar Medium (New York: Wiley)
Stevenson, D. J. 1981, Sci, 214, 611
Thuillier, G., Floyd, L., Woods, T. N., et al. 2004, in Solar Variability and its Effect on Climate Change, Geophysical Monograph 141, ed. J. M. Pap et al. (Washington, D.C.: Geophysical Union), 171
Tian, F. 2015, E&PSL, 432, 126
Tian, F., & Ida, S. 2015, in Pathways Towards Habitable Planets (Villeurbanne, France: Centre pour la Communication Scientifique Directe), 20
Tian, F., Kasting, J. F., & Zahnle, K. 2011, E&PSL, 308, 417
Tobie, G., Lunine, J. I., & Sotin, C. 2006, Natur, 440, 61
Tsuno, K., Frost, D. J., & Rubie, D. C. 2013, GeoRL, 40, 66
Turbet, M., Leconte, J., Selsis, F., et al. 2016, A&A, 596, A112
Udry, S., Bonfils, X., Delfosse, X., et al. 2007, A&A, 469, L43
Unterborn, C. T., Desch, S. J., Hinkel, N. R., & Lorenzo, A. 2018, Natur, in press, http://adsabs.harvard.edu/abs/2018NatAs.tmp...21U
Valencia, D., O'Connell, R. J., & Sasselov, D. D. 2007, ApJL, 670, L45
van Keken, P. E., Hacker, B. R., Syracuse, E. M., & Abers, G. A. 2011, JGRSE, 116, B01401
Venot, O., Hébrard, E., Agùndez, M., et al. 2012, A&A, 546, A43
Wadhwa, M. 2001, Sci, 291, 1527
Watson, A. J., Donahue, T. M., & Walker, J. C. G. 1981, Icar, 48, 150
Weller, M. B., & Lenardic, A. 2012, GeoRL, 39, L10202
Wheatley, P. J., Louden, T., Bourrier, V., Ehrenreich, D., & Gillon, M. 2017, MNRAS, 465, L74
Wordsworth, R. 2012, Icar, 219, 267
Wordsworth, R., Forget, F., & Eymet, V. 2010a, Icar, 210, 992
Wordsworth, R., Kalugina, Y., Lokshtanov, S., et al. 2017, GeoRL, 44, 665
Wordsworth, R., & Pierrehumbert, R. 2013, Sci, 339, 64
Wordsworth, R., & Pierrehumbert, R. 2014, ApJL, 785, L20
Wordsworth, R. D. 2016a, E&PSL, 447, 103
Wordsworth, R. D. 2016b, AREPS, 44, 381
Wordsworth, R. D., Forget, F., Selsis, F., et al. 2010b, A&A, 522, A22
Wordsworth, R. D., & Pierrehumbert, R. T. 2013, ApJ, 778, 154

Yeh, J. J. 1993, Atomic Calculation of Photoionization Cross-sections and Asymmetry Parameters (London: Gordon and Breach)
Yeh, J. J., & Lindau, I. 1985, ADNDT, 32, 1
Yelle, R. V. 2004, Icar, 170, 167
Yoshino, K., Esmond, J. R., Cheung, A. S-C., Freeman, D. E., & Parkinson, W. H. 1992, P&SS, 40, 185
Yung, Y. L., & DeMore, W. B. 1999, Photochemistry of Planetary Atmospheres, Vol. 1 (Oxford: Oxford Univ. Press)
Zahnle, K., & Catling, D. 2014, GSASP, 504, 37

Zahnle, K. J. 1986, JGRD, 91, 2819
Zahnle, K. J., & Catling, D. C. 2017, arXiv:1702.03386
Zahnle, K. J., Catling, D. C., & Claire, M. W. 2013, ChGeo, 362, 26
Zahnle, K. J., & Kasting, J. F. 1986, Icar, 68, 462
Zeng, L., & Sasselov, D. 2013, PASP, 125, 227
Zeng, L., Sasselov, D. D., & Jacobsen, S. B. 2016, ApJ, 819, 127
Zhang, H. L., Hirschmann, M. M., Cottrell, E., & Withers, A. C. 2017, GeCoA, 204, 83
Zolotov, M. Y., Sprague, A. L., Hauck, S. A., et al. 2013, JGRE, 118, 138